PE&RS
January 2023 Volume 89, Number 1

Photogrammetric Engineering & Remote Sensing *The official journal for imaging and geospatial information science and technology*

GEO WEEK

FEBRUARY 13-15, 2023
DENVER, CO - USA
geo-week.com

The intersection of **geospatial** + the **built world**

asprs THE IMAGING & GEOSPATIAL INFORMATION SOCIETY

Learn more!
geo-week.com/asprs

Geo Week is proud to partner with ASPRS to bring the ASPRS Annual Conference and exclusive workshops to Geo Week with sessions including:

- Ethical and Legal Concerns of AI-Driven Remote Sensing Applications
- Remote Sensing Data Quality and Interoperability Requirements
- Incorporating Lidar into Remote Sensing Projects
- Photogrammetric Processing and Applications
- Commercial Perspectives on the Uses of Imagery in GIS
- Guidelines and Standards for Topographic and Bathymetric Lidar
- Advanced Remote Sensing Analysis using Machine Learning and AI
- Revision of the ASPRS Positional Accuracy Standards for Geospatial Data
- Climate Change and Urban Analysis
- UAS Data Processing and Applications

ASPRS member discounts are available through the member portal. Geo Week conference passes can be purchased at an additional discount rate when bundled with the ASPRS Annual Conference Pass.

INDUSTRIES SERVED

Architecture, Engineering & Construction
Asset & Facility Management
Disaster & Emergency Response
Earth Observation & Satellite Applications
Energy & Utilities
Infrastructure & Transportation
Land & Natural Resource Management
Mining & Aggregates
Surveying & Mapping
Urban Planning/ Smart Cities

EVENT PARTNERS

asprs THE IMAGING & GEOSPATIAL INFORMATION SOCIETY
MAPPS
USIBD U.S. Institute of BUILDING DOCUMENTATION
WGIC World Geospatial Industry Council

Produced by diversified COMMUNICATIONS

To have your press release published in *PE&RS*, contact Rae Kelley, rkelley@asprs.org.

INDUSTRYNEWS

ANNOUNCEMENTS

NV5 Global, Inc., a provider of technology, conformity assessment, and consulting solutions, announced today that it has been awarded a $9 million contract by the National Oceanic and Atmospheric Administration's (NOAA) National Geodetic Survey to provide topobathymetric lidar, 4-band imagery, and mapping of the Maine shoreline.

Under the two-year contract, NV5 will deliver accurate and consistent measurement of the shoreline to support marine navigation safety, nautical charting, marine debris surveys, and marine resource management assessments. Geospatial data for the project will be obtained through topobathymetric lidar collection and processing and 4-band imagery of 3,115 sq miles of coastal Maine to provide views of both the shoreline and shallow water coastal area.

"We are pleased to continue our work with NOAA to support the accurate measurement of the nation's shoreline," said Dickerson Wright, PE, Chairman and CEO of NV5. "Our innovative work with topobathymetric lidar has made shoreline data acquisition possible in some of the most difficult coastal terrains and will support the work of marine industries and multiple government organizations."

For more information, visit https://www.nv5.com/geospatial/.

At the 2022 Technology Impact Awards in British Colombia, the Vancouver International Airport (YVR) recently received the Excellence in Industry Innovation Award by the BC Tech Association. The award-winning project involved a Digital Twin that was produced by GEO1 using **RIEGL** LiDAR and in partnership with GeoSim and Talon Helicopters.

A Digital Twin is a virtual representation that serves as the real-time digital counterpart of a physical object or process. Digital Twin models are being used at an increasing rate by airports to anticipate passenger movement and deploy resources, such as staff and vehicles, accordingly. They can also be used to develop simulations for training ground personnel and first responders, as well as to model emergency events or visualize future infrastructure development.

Once the data for YVR had been acquired by GEO1 with two RIEGL VUX-1LR Long Range Laser Scanners at an oblique angle to get improved coverage, the data could be stitched together by GeoSim to produce the final 3D model.

As the second largest airport in Canada, this Digital Twin allows YVR to be positioned at the forefront of innovation in the industry.

With an array of Phase One 150-megapixel cameras and RIEGL VUX-1LR Long Range Laser Scanners, the GEO1 team collected data at the rate of almost 1,000 megabytes per second.

For more information, visit https://newsroom.riegl.international/.

The U.S. Department of Agriculture (USDA) has consolidated several of its major geospatial programs under one new Blanket Purchase Agreement (BPA) called the PINE Aerial Imagery contract. As one of the award recipients, Surdex Corporation will provide geospatial services under five Farm Production and Conservation (FPAC) programs:

- National Agriculture Imagery Program (NAIP), a state-based orthoimagery program acquiring imagery during peak agricultural growing seasons.
- National Resource Inventory (NRI), a multi-agency, state-based program of high-resolution orthoimagery for the National Resource Conservation Service (NRCS).
- Stewardship Lands Inventory (SLI), an easement-based collection program for high-resolution orthoimagery supporting NRCS conservation easement programs.
- Resource, for collection of high-resolution orthoimagery for the USFS.
- Ad hoc and Disaster Support, which covers small to medium-sized areas identified for various USDA projects.

The 5-year PINE contract is being administered through the General Services Administration's (GSA) Multiple Award contract vehicle and will operate through mid-November of 2026.

For more information, visit https://www.surdex.com/blog/category/news/.

CALENDAR

- 27 January, **ASPRS GeoByte — Allen Coral Atlas: A New Technology for Coral Reef Conservation**. For more information, visit https://www.asprs.org/geobytes.html.
- 15-17 February, **ASPRS Annual Conference at Geo Week**, Denver, Colorado. For more information, visit https://my.asprs.org/2023conference.
- 5 May, **ASPRS GeoByte — SeaSketch 2.0: A New, Free and Open Source software Service for Map-based Surveys and Collaborative Geodesign.** For more information, visit https://www.asprs.org/geobytes.html.

PUBLISHING OPEN-ACCESS IN *PE&RS* IS NOW EASIER!

ASPRS is changing the subscription model of our monthly journal, *PE&RS*. ASPRS is waiving open-access fees for primary authors from subscribing institutions. Additionally, primary authors who are Individual Members of ASPRS will be able to publish one open-access article per year at no cost and will receive a 50% discount on open-access fees for additional articles.

- **Open Access matters!** By providing unrestricted access to research we can advance the geospatial industry and provide research that is available to everyone.
- **Institutions and authors receive more recognition!** Giving permission to everyone to read, share, reuse the research without asking for permission, as long as the author is credited.
- **Reputation matters!** Known for its high standards, *PE&RS* is the industry leading peer-review journal. Adding open access increases authors' visibility and reputation for quality research.
- **Fostering the geospatial industry!** Open access allows for sharing without restriction. Research is freely available to everyone without an embargo period.

Under the previous subscription model, authors and institutions paid $1500 or more in open-access fees per article. This will represent a significant cost savings. Open-access publications benefit authors through greater visibility of their work and conformance with open science mandates of funding agencies.

Subscriptions asprs.org/subscribe
Membership asprs.org/membership

asprs THE IMAGING & GEOSPATIAL INFORMATION SOCIETY

PE&RS
PHOTOGRAMMETRIC ENGINEERING & REMOTE SENSING
The official journal for imaging and geospatial information science and technology
January 2023 Volume 89 Number 1

COLUMNS

ANNOUNCEMENTS

DEPARTMENTS

See the Cover Description on Page 4

COVER DESCRIPTION

Along the coast of Senegal in West Africa, just a kilometer of beach separates the bright pink waters of Lake Retba from the dark blue-green waters of the Atlantic Ocean. But conditions at the lake (also called Lac Rose) are not always so rosy.

Located about 40 kilometers (25 miles) northeast of Dakar, Lake Retba attracts visitors who want to see its unique color and float in its salty, buoyant waters. With a concentration of salt that surpasses the Dead Sea, Lake Retba is also important to the local economy. Harvesters collect thousands of tons of salt from its waters each year, which is used locally for cooking and preserving food and is also exported to nearby countries.

The water's pink hue comes from Dunaliella salina—a single-celled algae that can tolerate salty environments. D. salina are a type of green algae, but under stressful conditions, such as high salinity or intense sunlight, they produce protective carotenoids, including orange-red beta carotene.

The lake is typically at its pinkest during the dry season (November to June) when there is persistent sunlight and high concentrations of salt. The top image, acquired by the Operational Land Imager (OLI) on Landsat 8, shows the lake on May 19, 2022, when waters appeared rosy.

The pink color fades during the region's wet season (July to October) when more clouds mean less sunlight and the waters become fresher due to rainwater. The bottom image, acquired with the Operational Land Imager-2 (OLI-2) on Landsat 9, shows the lake on September 16, 2022, when its color nearly matched the Atlantic Ocean.

The wet season in 2022 was especially wet. Bouts of torrential rain in early August and early September led to deadly flooding in Dakar and surrounding areas. The extreme rainfall impacted more than the lake's color; for example, floodwaters in September breached the lake's bank and washed away salt mounds that harvesters had collected there.

Lake Retba is the only pink lake in Africa, but the phenomenon occurs elsewhere around the planet. For example, Torrevieja Lagoon in Spain and Lonar Lake in India both take on rosy hues from the same single-celled algae.

NASA Earth Observatory images by Lauren Dauphin, using Landsat data from the U.S. Geological Survey. Story by Kathryn Hansen.

For more information, visit https://landsat.visibleearth.nasa.gov/view.php?id=150419.

asprs
THE IMAGING & GEOSPATIAL INFORMATION SOCIETY

PHOTOGRAMMETRIC ENGINEERING & REMOTE SENSING

JOURNAL STAFF

Publisher ASPRS
Editor-In-Chief Alper Yilmaz
Director of Publications Rae Kelley
Electronic Publications Manager/Graphic Artist Matthew Austin

Photogrammetric Engineering & Remote Sensing is the official journal of the American Society for Photogrammetry and Remote Sensing. It is devoted to the exchange of ideas and information about the applications of photogrammetry, remote sensing, and geographic information systems. The technical activities of the Society are conducted through the following Technical Divisions: Geographic Information Systems, Photogrammetric Applications, Lidar, Primary Data Acquisition, Professional Practice, Remote Sensing Applications, and Unmanned Autonomous Systems. Additional information on the functioning of the Technical Divisions and the Society can be found in the Yearbook issue of *PE&RS*.

All written correspondence should be directed to the American Society for Photogrammetry and Remote Sensing, PO Box 14713, Baton Rouge, LA 70898, including general inquiries, memberships, subscriptions, business and editorial matters, changes in address, manuscripts for publication, advertising, back issues, and publications. The telephone number of the Society Headquarters is 301-493-0290; the fax number is 225-408-4422; web address is www.asprs.org.

PE&RS. *PE&RS* (ISSN0099-1112) is published monthly by the American Society for Photogrammetry and Remote Sensing, 8550 United Plaza Blvd, Suite 1001, Baton Rouge, Louisiana 70809 . Periodicals postage paid at Bethesda, Maryland and at additional mailing offices.

SUBSCRIPTION. *PE&RS* is available as an e-Subscription (single-site and multi-site licenses) and an e-Subscription with print add-on (single-site license only). PE&RS subscriptions are on a calendar-year, beginning in January and ending in December.

The rate for a single-site e-Subscription for the USA/Non-USA is $1040 USD, for Canadian* is $1092 USD.

The rate for a multi-site e-Subscription for the USA/Non-USA is $1040 USD plus $250 USD for each additional license, for Canadian* is $1092 USD plus $263 for each additional license.

The rate for e-Subscription with print add-on for the USA is $1525 USD, for Canadian* is $1612 USD, and for Non-USA is $1565 USD.

*Note: Subscription prices for Canada includes 5% of the total amount for Canada's Goods and Services Tax (GST #135123065). **PLEASE NOTE: All Subscription Agencies receive a 20.00 USD discount.**

POSTMASTER. Send address changes to PE&RS, ASPRS, PO Box 14713, Baton Rouge, LA 70898. CDN CPM #(40020812).

MEMBERSHIP. Membership is open to any person actively engaged in the practice of photogrammetry, photointerpretation, remote sensing and geographic information systems; or who by means of education or profession is interested in the application or development of these arts and sciences. Membership is for one year, with renewal based on the anniversary date of the month joined. Membership Dues include a 12-month electronic subscription to *PE&RS*. Annual Individual Membership dues are $150.00 USD and Student Membership dues are $50.00 USD. A tax of 5% for Canada's Goods and Service Tax (GST #135123065) is applied to all members residing in Canada.

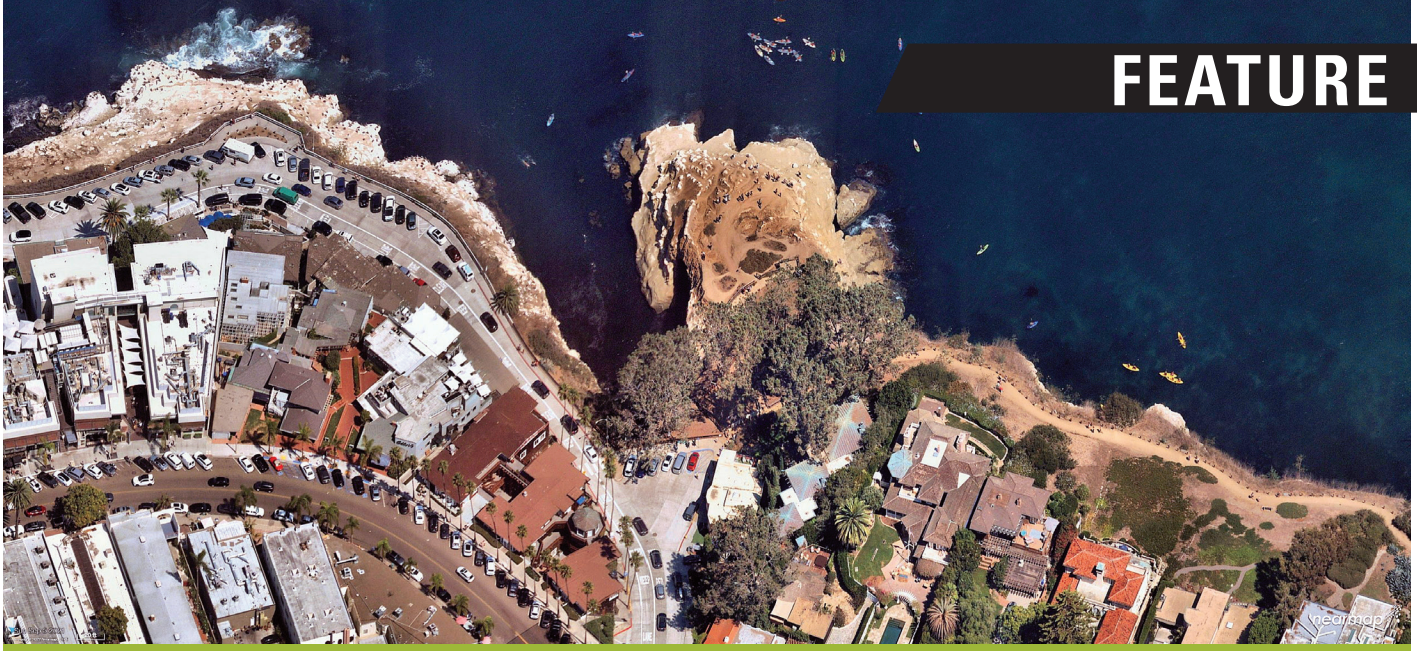

Aerial image provided by Nearmap of La Jolla, CA taken on 9/25/2021.

A Different Point-of-View
Using Aerial Imagery to Build Stronger Cities

By Shelly Carroll, Vice President and General Manager, Public Sector, Nearmap

When it comes to aerial imagery, city governments often make do with sporadically updated captures that fail to provide the most up-to-date information about the changing landscape of their urban areas. While they understand and appreciate the value of collecting this data, the update cadence is often too infrequent to reveal vital changes. As a result, information that is essential to successful planning and ongoing operations can go unrecorded and unanticipated.

This era of cities having to "make do" with self-collected aerial data may be coming to an end, thanks to new and enhanced photogrammetric products and possibilities. Increasingly, municipalities are realizing that frequently refreshed and consistent aerial imagery is a requirement if they are to keep pace with fast-growing and quickly evolving communities.

Sioux Falls Streamlines Assessments with Aerial Imagery

One recent example of this technology in action is happening in Sioux Falls, South Dakota, an Upper Midwestern city with a population of more than 200000. The most populous city in South Dakota, Sioux Falls accounts for more than 30% of the state's population.

Working with Nearmap, a leading aerial imagery and location intelligence company, Sioux Falls was able to streamline current assessment processes, leading to more accurate and easier-to-obtain data for their entire team of property assessors.

The company's premium geospatial content, combined with world-class mapping software and integrations, provided city assessors a consistent "source of truth" throughout the year. Armed with frequently refreshed images, the assessors were no longer constrained by the usual clutch of springtime image captures. Now they were able to review and assess based on late-season captures, as well, a time when many constructions projects near completion.

All data was openly accessible to anyone in the assessor's department with cloud-based access, allowing staffers to instantly stream imagery across devices. Easy integrations with CAD and GIS applications like Esri ArcGIS Pro were also essential for decision-makers from every municipal area, from public works employees to elected officials. The Sioux Falls team especially appreciated the ability to view current and historical imagery side-by-side, which is a feature of the Nearmap system that augments long-range planning activities.

City staff found that Nearmap's 3D Textured Mesh, a fully textured and colorized model, provided an enhanced understanding of actual conditions, which contributed to better informed decisions. Lauri Sohl, Civic Analytics Manager for the City of Sioux Falls, says, "While 3D urban models of proposed buildings are useful, combining them with Nearmap Textured Mesh gives people a true understanding of a project."

Photogrammetric Engineering & Remote Sensing
Vol. 89, No. 1, January 2023, pp. 5-8.
0099-1112/22/5-8

doi: 10.14358/PERS.89.1.5

Aerial image provided by Nearmap of Sun Lakes, AZ taken on 5/23/22

Breaking Down Silos for Smarter Cities

Many cities are finding that frequently updated imagery can break through existing departmental silos and support more efficient planning and operations throughout City Hall and beyond. Instead of relying on often-costly and inefficient bespoke aerial acquisitions, local governments are making the move to aerial capture programs, like the one in place in Sioux Falls. This way, users receive frequently refreshed high-resolution imagery and derived datasets that help them understand change at scale. Here's how municipal departments use these images:

- **Assessors** are able to conveniently and accurately inspect land, building structures, ground surfaces, and other taxable items for correct property valuations. They are able to remotely inspect parcels to identify new taxable activity and successfully defend against appeals.
- **Inspectors** rely on date-stamped aerial imagery to identify properties on which to focus attention. This reduces wasted trips to sites where, for example, construction has not yet begun or has slowed down mid-project.
- **Emergencies** require products like Nearmap's rapid ImpactResponse flights for the latest high-resolution basemaps to safely route police, fire, and response teams. Current aerial imagery is critical for coordinating actions on the ground, providing emergency staff a Common Operating Picture critical to developing strategy and coordinating tactics. And once the immediate danger of an emergency is over, teams can use the data to assess roof repairs, street blockages and other damage, accelerating the insurance claim process.
- **Transportation and road crews** can view even the smallest pavement irregularities – including potholes – with high-resolution, up-to-date aerial imagery. They can keep track of vegetation removal and planting projects, repairs, and they benefit from a bird's eye view of conditions as the seasons change. Officials can also use the imagery and 3D data to expand visibility into the material condition of assets like roads, vehicle depots, stations, rail tracks, bridges, pavement markings, and signage.
- **Public works, parks and recreation and environmental services** teams are able to work together seamlessly with a clear, current and consistent source of truth. For example, aerial imagery and derived datasets enable measurement and assessment of trees and greenspaces over time. For areas under water restrictions, officials can identify and monitor areas of concern that may indicate unauthorized use of scarce water resources.
- **Water, electricity, waste, and environmental utilities** use high-resolution aerial basemaps to track infrastructure, deploy crews efficiently, and respond quickly to interruptions. Large utility inventories can be quickly tracked through feature extraction and measurement of assets like electric distribution lines and poles, manholes, and water features. Potential risks to power lines or other vulnerable infrastructure from vegetation can be highlighted through historical image reviews.
- **City council, mayor, and other elected officials** value the presentation of planning materials that use GIS-integrated, high resolution recent aerial imagery to showcase environmental, social, and governance (ESG) trends. Policy development may be malinformed without the insights of location-based intelligence. And the common vision provided by recent aerial imagery is critical to a successful public input process.
- **Residents** are likely to be more engaged when better equipped with information that is easy to access and understand. Updates about the progress of road construction, new sidewalks, or park improvements can make planning their days easier. Cities are finding that communicating more accurate projections about projects helps gain public acceptance and green-light planned future efforts.

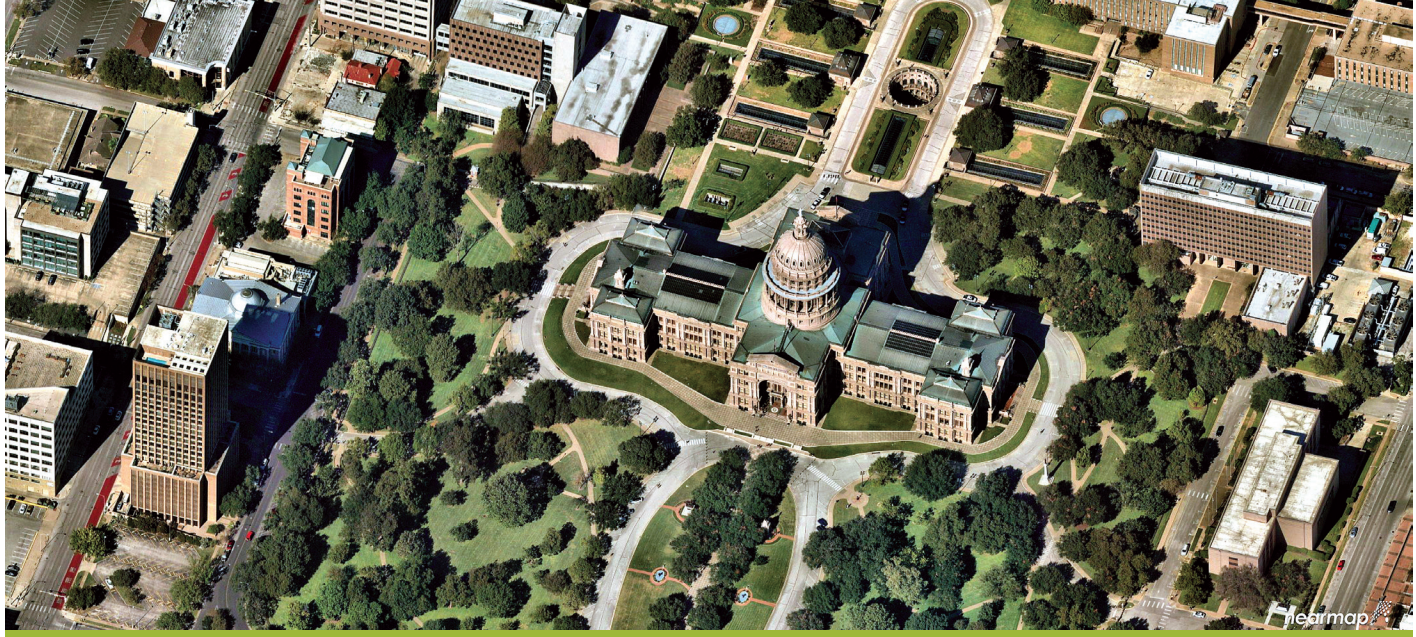

Aerial image provided by Nearmap of the Texas State Capitol taken on 10/30/2021.

How it Works

Nearmap proactively acquires and processes aerial imagery and positional data, providing subscription-based access to an ever-growing library of geospatial content. Over 80% of the U.S. parcel base is captured annually at a frequency of up to three times per year. The Nearmap ImpactResponse Program focuses on areas of natural disaster, prepositioning resources and acquiring imagery immediately following flood, wind, fire, and other events. Rounding out the acquisition offerings is the NearmapNow Program, which allows customers to obtain custom flights. In 2022, these three programs captured data for over 1.7 million square kilometers across North America.

Nearmap has built and owns its entire technology stack, from sensing systems to processing pipelines through delivery solutions. This patented digital "ecosystem" optimizes the quality, consistency, and speed of deliverables while minimizing the operational risk associated with capturing petabytes of data globally.

HyperCamera 2, the current generation of camera system, captures vertical imagery at a Ground Sample Distance (GSD) of 5.5cm (2.2") and horizontal accuracy of 19.8cm (7.8"). Oblique imagery and positional data are acquired concurrently. A full compliment of 3D content and Artificial-Intelligence (AI)-derived data layers result from each capture: textured mesh, Digital Surface Models (DSMs), point clouds,

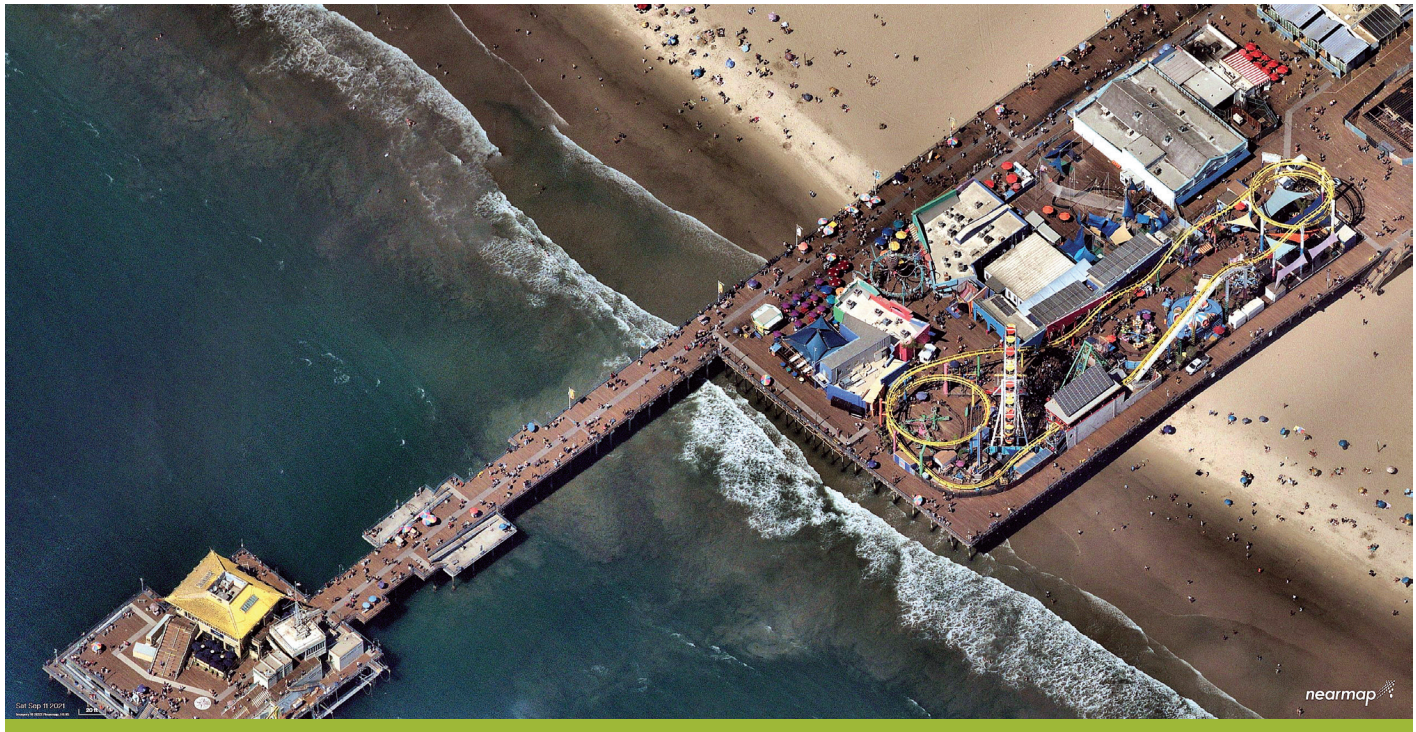

Aerial image provided by Nearmap of Santa Monica Pier, CA taken on 9/11/2021.

Aerial image provided by Nearmap of Red River Showdown in TX, taken on 10/9/2021.

and over 75 thematic vector datasets. HyperCamera 3 will debut in spring of 2023, with technological advances that significantly enhance spatial and spectral resolution, as well as the processed deliverables.

Nearmap's cloud-based photogrammetry pipeline generates these products for streamed access to customers within days of capture. Integration with GIS, CAD, Asset Management, and other decision support systems is seamless, enriching their content and context. The imagery, 3D, and AI content serves as source of truth to power a government's common operating picture (COP), allowing cities to maximize the value of all their location intelligence assets.

City Officials Weigh In

For cities that have made the move to frequently captured high-quality aerial imagery, the improvement is notable. They have been able to embrace change and build a more sustainable future by relying on the more current geospatial information.

For Trisha Favulli, Director of Assessing for Falmouth, Massachusetts, the move to more frequent aerial data has allowed her town to get ahead of a serious assessment backlog. "Before Nearmap, we were already two years behind on our imagery capture through our county commission. With Nearmap, my view has never been clearer or more up-to-date."

Timothy Zimmer, the GIS Administrator for Shelby County 911 in the Memphis metropolitan area, is impressed with the overall improvement of the accuracy of the information he can now access any time, from any connected device. "I really like how Nearmap is integrated into the GIS stack," he says. "We are able to stay on top of new developments, roads, and addresses. And being able to have Nearmap imagery integrated into our GIS systems helps us to be much more accurate."

The frequency of information updates has made a difference for Matthew W. Bradbury, GIS Administrator for the City of Redlands, California. "Nearmap affords us the ability of a bird's-eye view of our city not just once a year, but several times per year, at a resolution that is rarely obtainable within our budget," he says.

The Future is Now

Cities of the past often operated within clearly defined departmental silos that limited knowledge-sharing and mutually beneficial planning opportunities. Street crews might dig up and resurface a major road, unaware that the water utility teams had a pipe-replacement project planned for the area six months later. The street closures required for a city festival might not be effectively communicated to traffic, public works, or sanitation crews. And citizens might feel confused about the purpose and status of city improvement projects, or blindsided by changes proposed for their neighborhood.

Today, cities supported by frequently updated imagery are able to operate with a more data-driven mindset. High resolution imagery and derived data encourage a Common Operating Picture, from which everyone can share knowledge, and in which cities can grow and thrive, fueled by an understanding of the history and the changes within their boundaries.

About the Author

Shelly Carroll, shelly.carroll@nearmap.com, is the Vice President and General Manager, Public Sector of Nearmap. She has served the geospatial profession for over 25 years in both the public and private sector. Her expertise includes planning, emergency response, and resiliency. She holds the accreditation in Agile Certified Practitioner (ACP), Certified Business Analyst Professional (CBAP), Project Management Professional (PMP). Nearmap, 10897 S River Front Pkwy, South Jordan, UT 84095.

GIS Tips & Tricks

Al Karlin, Ph.D. CMS-L, GISP

When is Sharing not Sharing?

If you have been following this column, you know that I often draw my tips and tricks from student questions in my GIS class. This month's tips originate in what I thought would be a simple assignment at the beginning of the semester.

Background

My class is comprised typically of students from various backgrounds, academic-level (Sophomores through Seniors although an occasion Freshman sneaks in), and disciplines, some technical (think marine science or environmental science), some from the social sciences (think sociology or history) and some from the business school (think business management.) Most, are familiar with their personal computers, but, that computer happens to be some flavor of a MacBook running some version of MacOS X. The "gottcha" is that in the GIS laboratory, the university is running Esri-ArcGIS Pro (v2.9) on Windows 10x64 computers. So, what would appear to be a simple task for a Windows 10x64 user, turns out to be a pretty complex assignment for most of my beginning GIS students.

The Assignment

At your choice of GIS-data rich websites (I provided six URLs to websites in the state), download 3 (or more) datasets, add each to a Map Frame, symbolize each in whatever makes sense to you, construct a layer package, and upload that package the class DropBox folder (all students have access to class DropBox folders.)

After being deluged by student e-mails asking for help, here are my tips:

Tip #1 — When downloading GIS data files, the most common data exchange format is an Esri Shapefile (we actually discuss this in class and the need for four computer files.) The files; a .shp, .shx, .dbf, .prj, etc. are usually archived into a single ZIPped (.zip) file for downloading. The Esri ArcGIS Pro file browser recognizes the .zip format BUT when attempting to open a ZIPped file archive, it appears empty to the Esri file browser. The ZIPped archive must be unzipped using the Windows Operating System (or a dedicated, third-party software program) before ArcGIS can read the files and construct a layer. Of course, unZIPping a file is as easy as clicking on the file and selecting the "Extract All" function on the Windows 10 ribbon. Functionality not commonly used in the MacOS environment.

Tip#2—Adding a shapefile to a Map Frame is as easy as selecting the .shp file from a Windows file browser (left-clicking on it) and dragging (holding down the left mouse-button) the selected file onto the Map Frame.

However, quickly looking at the Windows File Browser will show two .shp files as shown in Figure 1. Careful inspection reveals that one is a SHP file while the other is an XML Document Selecting and dragging the XML Document file (immediately below the SHP file in Figure 1) onto a Map Frame will result in an "Add data" error (Figure 2.)

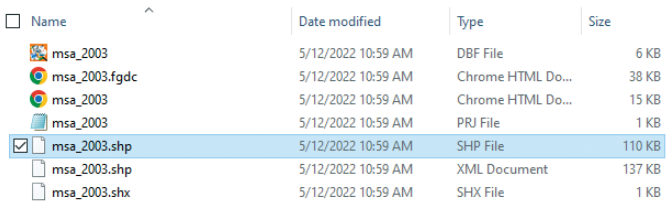

Figure 1. The SHP file for this GIS dataset is highlighted. It can be selected and dragged onto an ArcGIS Pro Map Frame. Dragging the XML Document file, also with the .shp extension, as shown immediately below the highlighted file, onto the Map Frame will result in an error (Figure 2.)

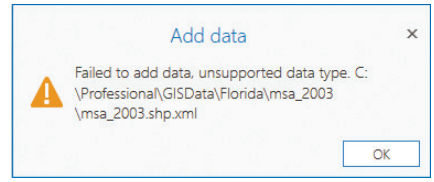

Figure 2. This error will result when the XML Document file is selected and dragged onto an ArcGIS Pro Map Frame.

Alternatively, you can attach to a folder in either Catalog or the Map Frame (Insert | Add Folder) and navigate through the ArcGIS Pro file browser interface. Again, navigation through a file structure is not common in the MacOS environment. (Note: If the feature classes are already contained in a GeoDatabase, then just dragging the feature class onto the Map Frame adds it to the Contents pane.)

Photogrammetric Engineering & Remote Sensing
Vol. 89, No. 1, January 2023, pp. 9-11.
0099-1112/22/9-11

doi: 10.14358/PERS.89.1.9

Tip #3 — Creating a Group is as easy as selecting the all the desired layers (holding the <CTRL> down and left clicking on the layers) in the Contents Pane and then right-clicking and selecting "Group" from the options menu (Figure 3.)

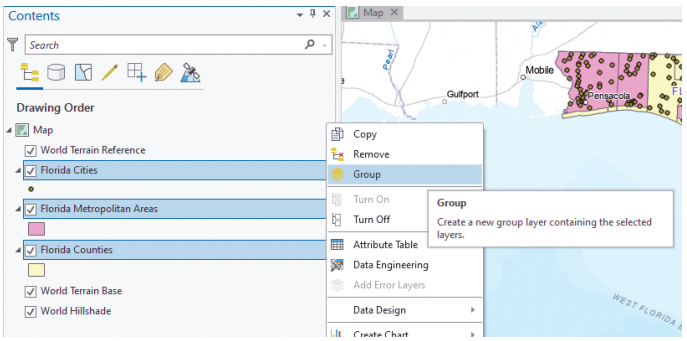

Figure 3. Selecting multiple layers in the Contents Pane and constructing a Group Layer.

Alternatively, Selecting the Map in the Contents Frame, and right-clicking activates the options menu where you can select "New Group Layer". In either case, name the New Group Layer and drag the layers into the group as needed. Another function not found in the MacOS environment.

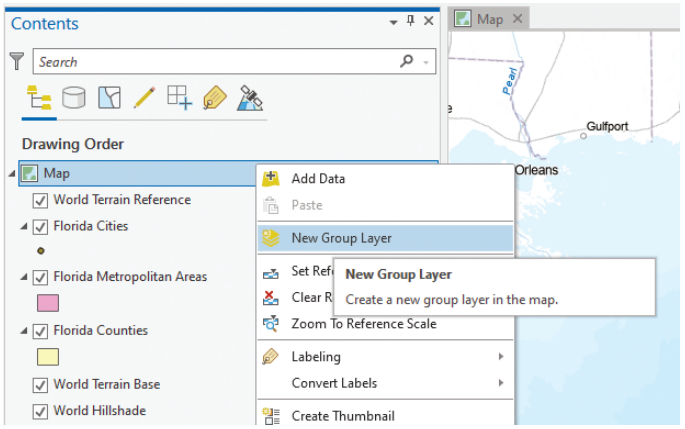

Figure 4. Constructing an empty Group Layer from the Map options.

Tip #4 — In the Esri-world, making (and saving) a Layer Package is called "Sharing". This was a source of endless confusion, as I told the students to make, save the package, and send it to our DropBox for me to review. Most were trying to "save" something, but they did not know what (or how) to save.

Right-clicking on the Group Layer presents several options including the "Share As Layer Package" as in Figure 5.

Selecting the "Share As a Layer Package" will start the "Sharing As A Layer Package" wizard (Figure 6). In the Start Packaging section, make sure to select the "Save package to file" radio button; then, in the Item Details | Name field use the folder to open the file browser and navigate to a writable folder to specify an output file path and name. To prevent errors and warnings, also include a Summary and some Tags. In the Finish Packaging section, use the "Analyze" button to check the file before using the "Package" button to SHARE (=Save) the Layer Package. Of course, if there are any errors, you will need to fix them before you can Package the Layer Package.

Once everything is error-free, it may take a few moments to write the package and finally the Layer Package (Figure 7) will be ready for others to use. This file can be sent to other ArcGIS Pro users for inclusion in their maps. It contains the GIS data, as well as, assigned symbology.

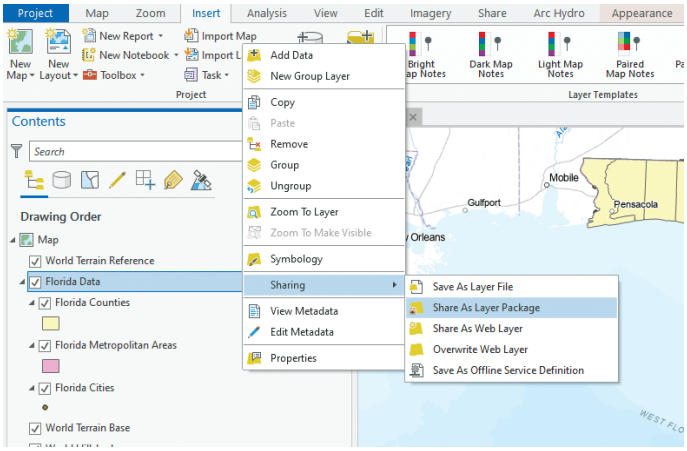

Figure 5. The options menu for a Group Layer shows the "Sharing" options. There is no "save" choice on the options menu.

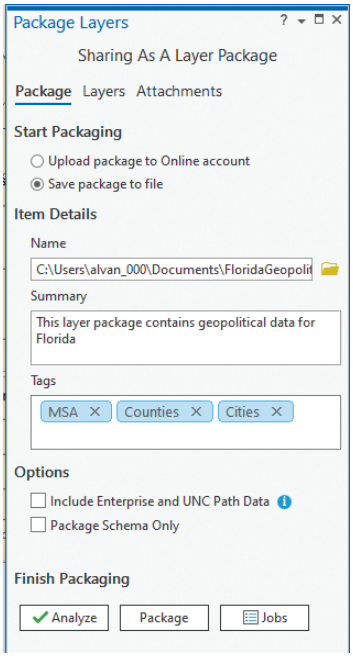

Figure 6. The Package Layers | Sharing as a Layer Package wizard. If wanting to "save" the Layer Package, it is necessary to activate the "Save Package to File" radio button.

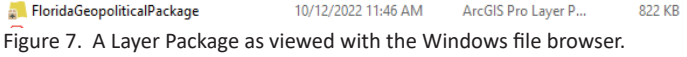

Figure 7. A Layer Package as viewed with the Windows file browser.

For those of you who use QGIS, similar functionality can be achieved using the following workflow:

1. Symbolize the layers in the QGIS Layers Pane,
2. Select the desired layers (left-click while holding down the <CTRL> Key),
3. Right-click in the Layers Pane to activate the options and choose "Group Selected" as in Figure 8,
4. Rename the Group Layer,
5. Select and Export the Group Layer | Save as Layer Definition File. This will start a file browser; browse to a writable directory and write the .qlr file.

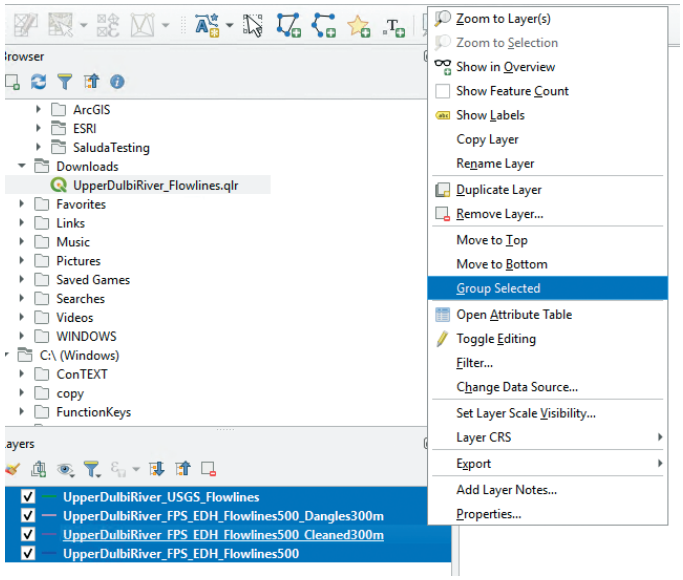

Figure 8. Selecting four layers in the QGIS Layer Pane for grouping.

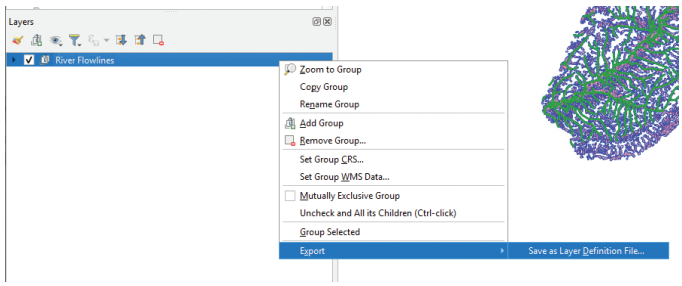

Figure 9. Exporting (saving) the Grouped Layers as a Layer Definition File in QGIS.

As with the Esri-derived layer package (.lpkx) file, this QGIS-derived layer package (.qlr) file contains the geometry, symbology and can be ported into another QGIS map frame. It is important to note that these files are NOT interchangeable; ArcGIS Pro cannot draw the QGIS layer package and vice versa.

Send your questions, comments, and tips to GISTT@ASPRS.org.

Al Karlin, Ph.D., CMS-L, GISP is with Dewberry's Geospatial and Technology Services group in Tampa, FL. As a senior geospatial scientist, Al works with all aspects of Lidar, remote sensing, photogrammetry, and GIS-related projects. He also teaches beginning map making at the University of Tampa.

ASPRS GeoByte

Allen Coral Atlas: A New Technology for Coral Reef Conservation

September 23rd at 12 Noon ET

Presenter: Brianna Bambic, *Arizona State University*

Coral reef managers and decision makers at multiple scales need information, in near real time, to react to the increasing threats facing reefs. However, more than three quarters of the world's coral reefs have never been mapped and lack monitoring. To address this knowledge gap and to support, inform, and inspire critical actions to manage and protect coral reefs, the Allen Coral Atlas combines high resolution satellite imagery, machine learning, and field data to produce globally consistent benthic and geomorphic maps and monitoring systems of the world's coral reefs. The initiative's goal is to help stakeholders ranging from local communities to regional and national governments reach their conservation targets and improve their coastal resilience. The multi-disciplinary partnership is led by Arizona State University, in collaboration with Planet, University of Queensland, and the Coral Reef Alliance.

Baseline maps have multiple uses, including: sustainable coastal development, site selection of marine protected areas, planning of restoration activities, and reef fisheries management. In this presentation, we will demonstrate how the Allen Coral Atlas supports data-driven management, conservation, and restoration of coral reefs at local, national, regional, and global scales. We have developed online courses to facilitate increased use and impact of the Atlas, and are collaborating with networks of individuals and institutions who can be alerted when changes are detected (e.g., large-scale bleaching or sedimentation events).

Brianna Bambic leads the Allen Coral Atlas Field Engagement team at the Arizona State University. With a coral reef biology and resource management background, she was an Independent Researcher for 7 years that culminated in a virtual reality experience of Half Moon Caye National Monument, Belize with a National Geographic Explorer Grant, helping communicate science to the public. Brianna received her MS in natural resource management from the University of Akureyri, Iceland in 2019. Her expertise includes coastal and marine management, global science communication, and developing capacity around remote sensing and mapping. With countless hours underwater and >700 logged dives, she loves spending time exploring the ocean..

To register, visit
https://www.asprs.org/geobytes.html

STAND OUT FROM THE REST

EARN ASPRS CERTIFICATION

ASPRS congratulates these recently Certified and Re-certified individuals:

CERTIFIED LIDAR TECHNOLOGIST

Christina Gray, Certification #LT076
Effective October 26, 2022, expires October 26, 2025

Thomas Rokita, Certification #LT077
Effective September 14, 2022, expires September 14, 2025

CERTIFIED MAPPING SCIENTIST GIS/LIS

Gabriel Ladd, Certification #GS313
Effective November 2, 2022, expires November 2, 2027

CERTIFIED MAPPING SCIENTIST – REMOTE SENSING

Su Zhang, Certification #RS240
Effective October 20, 2022, expires October 20, 2027

Gabriel Ladd, Certification #RS241
Effective November 1, 2022, expires November 1, 2027

CERTIFIED PHOTOGRAMMETRIST

Gabriel Ladd, Certification #CP1670
Effective October 26, 2022, expires October 26, 2027

Gregory Saunders, Certification #CP1671
Effective November 16, 2022, expires November 16, 2027

RECERTIFIED LIDAR TECHNOLOGIST

Ciaran Manning, Certification #R047LT
Effective November 7, 2022, expires November 7, 2025

Greg Jackson, Certification #R004LT
Effective February 1, 2022, expires February 1, 2025

RECERTIFIED PHOTOGRAMMETRIST

David Walls, Certification #R1338CP
Effective November 17, 2022, expires November 17, 2027

Mohannad Al-Durgham, Certification #R1621CP
Effective August 11, 2022, expires August 12, 2027

Douglas Lee Smith, Certification #R1090CP
Effective March 21, 2022, expires March 21, 2027

Edward Kaster, Certification #R1624CP
Effective October 10, 2022, expires October 10, 2027

Paul J. Emilius, Jr., Certification #R994CP
Effective March 1, 2022, expires March 1, 2027

Jessica S. Parsons, Certification #R1536CP
Effective November 25, 2022, expires November 25, 2027

Michael J. Lalla, Certification #R1511CP
Effective October 21, 2022, expires October 21, 2026

Timothy M. Bohn, Certification #R1207CP
Effective October 18, 2022, expires October 18, 2027

Jon Dewald, Certification #R1535CP
Effective November 18, 2022, expires November 18, 2027

Michael Rodger, Certification #R1330CP
Effective May 23, 2022, expires May 23, 2027

RECERTIFIED MAPPING SCIENTIST UAS

Cody Condron, Certification #R001UAS
Effective November 3, 2022, expires November 3, 2027

Gabriel Ladd, Certification #UAS039
Effective November 17, 2022, expires November 17, 2027

Josh Kowalski, Certification #UAS040
Effective October 19, 2022, expires October 19, 2027

RECERTIFIED MAPPING SCIENTIST REMOTE SENSING

Chuan-Shin Chong, Certification #R235RS
Effective May 19, 2022, expires May 19, 2027

RECERTIFIED MAPPING SCIENTIST GIS/LIS

Robert E. Davis, Certification #R292GS
Effective September 27, 2022, September 27, 2027

Stephen Ellis, Certification #R258GS
Effective October 19, 2022, expires October 19, 2027

RECERTIFIED MAPPING SCIENTIST UAS

Zachary Radel, Certification #R009UAS
Effective November 3, 2022, expires November 3, 2027

Stefan Claesson, Certification #R003UAS
Effective November 3, 2022, expires November 3, 2027

ASPRS Certification validates your professional practice and experience. It differentiates you from others in the profession. For more information on the ASPRS Certification program: contact **certification@asprs.org,** visit **https://www.asprs.org/general/asprs-certification-program.html.**

& Grids & Datums

Democratic Republic of the Congo

BY Clifford J. Mugnier, CP, CMS, FASPRS

The Grids & Datums column has completed an exploration of every country on the Earth. For those who did not get to enjoy this world tour the first time, *PE&RS* is reprinting prior articles from the column. This month's article on the Democratic Republic of the Congo was originally printed in 2005 but contains updates to their coordinate system since then.

The Democratic Republic of the Congo (Kinshasa), formerly called Zaire and prior to that, the Belgian Congo, lies on the equator and has borders with the Republic of Congo (Brazzaville) 2,410 km, the Central African Republic 1,577 km, Sudan 628 km, Uganda 765 km, Rwanda 217 km, Burundi 233 km, Tanzania 459 km, Zambia 1,930 km (*PE&RS*, October 2004), Angola 2,511 km (*PE&RS*, March 2001), and a small coastline on the Atlantic. The central region has an equatorial climate with high temperatures and heavy rainfall, with different climatic cycles in the northern and the southern regions. French is the offcial language, and Christianity is the majority religion. Archaeological evidence of past societies in the Congo are scanty due to the rain forest and tropical climate covering the northern half of the country and much of the Congo River Basin. Equatorial Africa has been inhabited since at least the Middle Stone Age. Late Stone Age cultures flourished in the southern savanna from approximately 10,000 *B.C.* and remained until the arrival of Bantu-speaking peoples during the first millennium *B.C.*

Comprising an area of slightly less than one-fourth of the United States, the country has a 37 km coastline with a 12 nm territorial sea. The terrain is a vast central basin on a low-lying plateau with mountains in the east. The lowest point is the Atlantic Ocean (0 m), and the highest point is Pic Marguerite on Mont Ngaliema or Mount Stanley (5,110 m).

From the Office of the Geographer, U.S. Department of State in International Boundary Study No. 127,

"Initially France established claims in the Congo

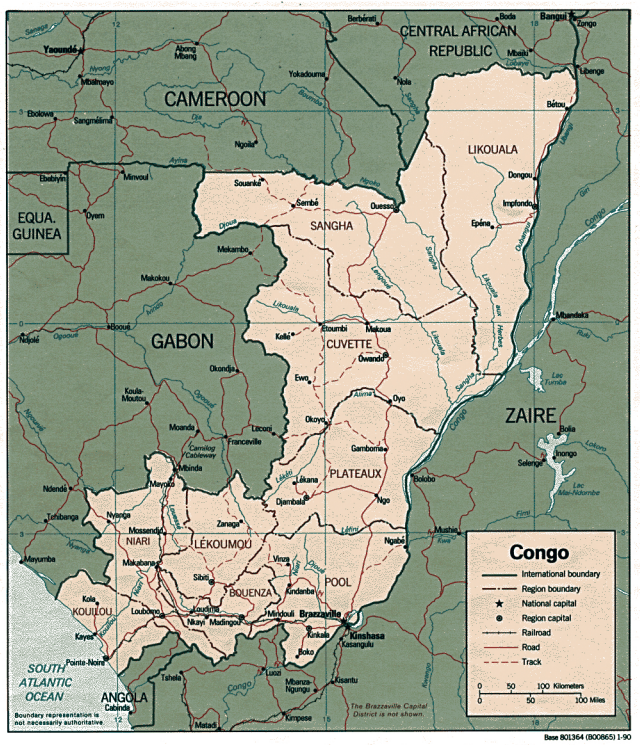

basin through penetration of the territory from bases in Gabon and by treaties with local rulers. In a series of expeditions between 1875 and 1882, Pierre Savorgnan de Brazza, an officer of the French navy, explored much of the territory between the Ogooué and Congo rivers including the Niari valley. In 1880 de Brazza negotiated a treaty with the ruler of the Teke kingdom, which secured part of the north bank of the Congo for France, but because of quiet anchorage, he constructed a station on Kintamo Island near the south bank.

During this period with an expedition from East Africa, the explorer Henry M. Stanley descended the Congo River to its mouth in 1877. King Leopold

Photogrammetric Engineering & Remote Sensing
Vol. 89, No. 1, January 2023, pp. 13-15.
0099-1112/22/13-15

doi: 10.14358/PERS.89.1.13

II of Belgium later retained his services to establish stations and to make treaties with the people of the Congo basin. In 1881 de Brazza met Stanley who was advancing eastward thorough the cataract area of the lower Congo River. Stanley arrived in the vicinity of Stanley Pool (Pool Malebo) on July 27 of the same year and founded Léopoldville on the south bank of the Congo at the site of present-day Kinshasa. Shortly thereafter, the French post on Kintamo Island was moved to the north bank of the Congo, where it became known as Brazzaville. …"

"In the meantime, King Leopold had shown great interest in the development of Africa. He invited explorers, geographers, and philanthropists of various states to a conference on central Africa at Brussels on September 12, 1876. An African International Association was organized at the conference with headquarters at Brussels. It was agreed that branches of the association in various states would be known as national committees, and King Leopold headed the Belgian National Committee.

Following the historic trip of Stanley down the Congo in 1877, King Leopold shifted his primary interests in tropical Africa from the east to the west coast. Therefore, in 1878 another committee was organized under the title of the Committee for Upper Congo Studies, which later was known as the International Association of the Congo. The association was in effect a development company with King Leopold being the principal stockholder, and Stanley was commissioned by the King for service under the International Association of the Congo. Between 1879 and 1882, Stanley established stations and made treaties with numerous African chiefs, many of which were in the upper part of the Congo basin.

Early in 1884 several states recognized the Association as a governing power on the Congo River. In an exchange of notes between France and the Association of the Congo, April-May 1884, France was accorded the right of preemption of preferential right to the region of the Congo and in the valley of Niadi-Quillou (Niara-Kouilou) should the Association of the Congo dispose of its territorial possessions.

The Berlin Conference of 1884-1885 recognized King Leopold as the sovereign head of state for the International Association of the Congo. On July 1, 1885 the name of the entity was changed to the Congo Free State, which was retained until it became a Belgian colony in 1908. A treaty for the cession of the Congo Free State to Belgium was signed at Brussels on January 9, 1895, and submitted to the Belgian Chamber of Deputies for approval shortly thereafter; however, it was withdrawn without any formal action being taken. An arrangement made between Belgium and France relative to the French right of preemption of a Belgian colony of the Congo was signed at Paris on February 5, 1895, but it was not ratified in consequence of the withdrawal of the treaty of cession. A second treaty for the cession of the Congo Free State to Belgium was signed on November 28, 1907, and approved by a Belgian Law of October 18, 1908. The treaty of cession was followed by an arrangement between Belgium and France governing the French preferential right to the Belgian Congo on December 23, 1908."

The first geodetic surveys in the Congo were part of the 1911-1914 boundary survey between Northern Rhodesia (now Zambia) and the southern Congolese province of Katanga. The fundamental (origin) point of the Katanga Triangulation is Station "A" of the Tshinsenda baseline (in Zambia) [Chain I], where: $\Phi_o = 12^o\ 20'\ 31.508''$ S and $\Lambda_o = 28^o\ 01'\ 02.465''$ E. The altitude of the point was 1,331.31 m, as determined by trigonometric leveling from the 30th Arc triangulation performed in 1912. The ellipsoid of reference used by the Belgians for the computation of the triangulation in Katanga Province was the Clarke 1866 where: a = 6,378,206.4 m, and b = 6,356,583.8 m. They also referenced the Clarke 1866 Tables as published by the U.S. Coast & Geodetic Survey. In 1954, *Comité Spécial du Katanga, Les Travaux Géodésiques du Service Géographique et Géologique* was published. The Tshinsenda Baseline [Chain I], was measured in 1912 with a length of 4,152.9912 m with the final value being adjusted with the 1923 base at Nyanza, both surveyed by the Katanga-Rhodesia Boundary Commission. The deflection of the vertical was constrained to zero at point "A." Subsequent geodetic survey connections to the Katanga triangulation by the Arc 1950 Datum provided a couple of common points. I computed the transformation from the Katanga Datum of 1912 to the Arc 1950 Datum as: ΔX = +44 m, ΔY = +46 m, ΔZ = +34 m, and I would guess that for southern Katanga these parameters are good to ±25 m. The projection adopted for the general map of Katanga was the Lambert Conical Orthomorphic with two standard parallels at $\varphi_N = 6^o\ 30'$ S and $\varphi_S = 11^o\ 30'$ S and a central meridian, $\lambda_o = 26^o$ E. However, the reason why such emphasis was placed on the province to begin with was the presence of large deposits of copper ore. With mining property values being high, a cadastral coordinate system was implemented at the same time such that a Gauss-Krüger Transverse Mercator grid was defined with a central meridian, $\lambda_o = 26^o$ E and a False Northing Latitude of Origin = 9° S and the Scale Factor at Origin = 0.9998.

The classical triangulation of Katanga required a number of baselines to be measured in order to provide a uniform reference scale to the datum. Those baselines, in addition to the 1912 Tshinsenda distance included: Kitanga

(1922) [Chain II], 3,695.0250 m, Mutene (1922)[Chain III], 1,554.9333 m, Nyanza (1923) [Chain XI], 4,881.8892 m, Kilambo (1929) [Chain VI], 6,601.2811 m, Pweto (1929) [Chain IX], 5,018.0550 m, Bululwe (1923) [Chain VIII], 10,516.9679 m, Gandajika (1947) [Chain XIII], 12,955.3016 m, and Kita Mulambo (1951) [Chain XIV], 9,187.7147 m.

An interesting "faux pas" in geodetic lore is the "Gan Datum" of the Congo. The Gandajika baseline was noticed by someone in the DMA and was confused with the Maldives Island of "Gan." As a result, the actual datum transformation for the island of Gan was incorrectly attributed to the Katanga region of Congo (Kinshasa), which has since been rectified. There is no "Gan Datum" in the Congo. I wonder what is left of the true Indian Ocean Gan Datum after the catastrophic tsunami of December 26, 2004!

The published relation between Arc 1950 Datum and WGS84 Datum in the Congo (Kinshasa) by the NGA is as follows: $\Delta X = -169$ m± 25 m, $\Delta Y = -19$m ± 25 m, $\Delta Z = -278$ m ± 25m, and this solution was based on 2 points in 1991. The current grid system used for the People's Republic of the Congo (Kinshasa) is the UTM.

Thanks to Melita Kennedy of ESRI for prodding me for answers on the legendary "Gandajika Datum," to John W. Hager for the answers on the history of the same legend, and to Mal Jones of Perth, Australia for the source material on the triangulation of Katanga. I am informed that a GPS Survey of the Congo (Kinshasa) is currently in the planning stages by private concerns.

Democratic Republic of the Congo (Kinshasa) Update

In 2009, the Kinshasa government published a law delimiting the maritime area of the Democratic Republic of the Congo. (https://www.un.org/depts/los/LEGISLATIONANDTREATIES/PDFFILES/cod_2009_law09.pdf) "On the basis, in particular, of article 9, paragraph 1, of the Constitution of 18 February 2006 which asserts the permanent sovereignty of the Democratic Republic of the Congo over its maritime areas, and on the basis of the relevant provisions of the United Nations Convention on the Law of the Sea of 1982, the present law establishes the maritime borders and enshrines the country's fundamental right to those maritime areas." The charts used for the development of the defining points are navigation charts which presumably are cast on the Normal Mercator projection, and therefore by definition the straight lines are ellipsoidal loxodromes on the WGS84 Datum.

The enumeration of the various points were computed in compliance with International Laws of the Seas (LOTS) using public-domain software written by Teledyne Geospatial. The software is called "CARIS" and is apparently available from: https://www.teledynecaris.com/en/products/easy-view/.

This column was previously published in *PE&RS*.

Look for

ASPRS Ten-Year Industry Remote Sensing Industry Forecast Highlights

in future *PE&RS* issues

- ASPRS Ten-Year Industry Remote Sensing Industry Forecast Survey continues and builds on the practice started in the late 1990s to understand the trends and directions of the industry
- ASPRS established the 10-year forecast with the civil government and its broad-based remote sensing membership
- Your remote sensing inputs are very important in shaping the future
  - To document remote sensing needs and trends
  - To drive current and future requirements and funding
- Take the survey today: **https://calval.cr.usgs.gov/apps/asprs_survey**
- Publication and online financial sponsors will be acknowledged in the publication
- Any questions, support, or sponsor requests can be provided to: **PDAD email, divisiondirectorspdad@asprs.org**

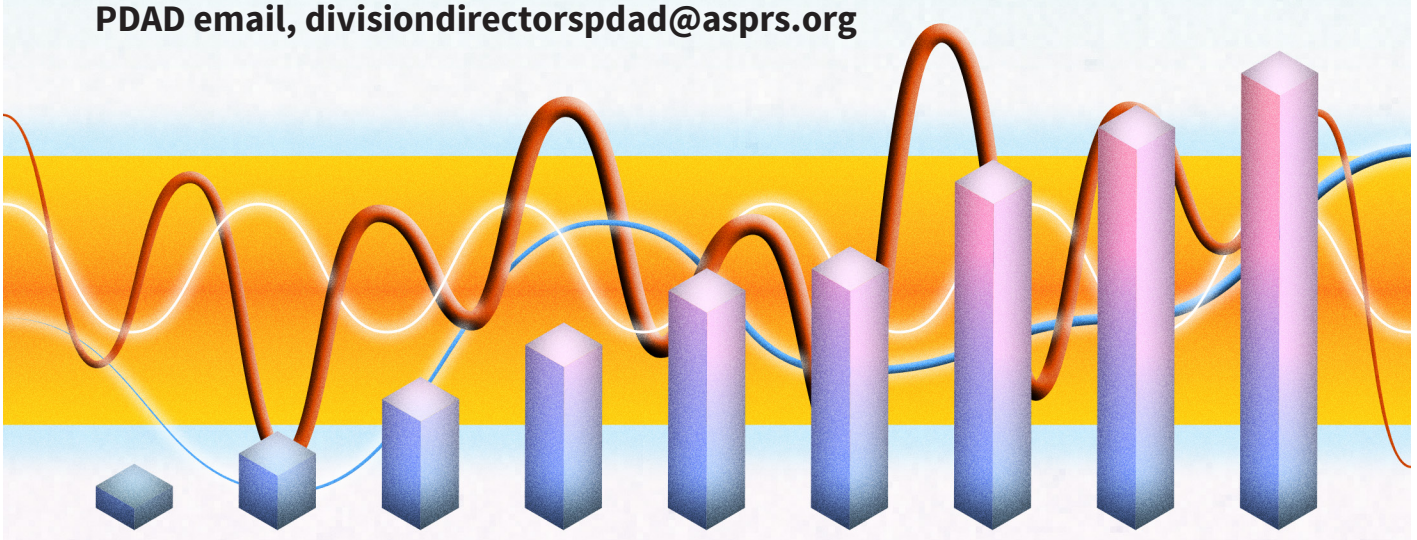

asprs THE IMAGING & GEOSPATIAL INFORMATION SOCIETY

ANNOUNCING THE 2023 ASPRS ELECTION RESULTS

Join us at the Installation of Officers on Wednesday, February 16 at 8:00 AM MST at Geo Week 2023!

Amr Abd-Elrahman,
Vice President

Matt Elious,
Assistant Director,
Professional Practice
Division

Ravi Soneja,
Assistant Director, Primary
Data Acquisition Division

Indu Jeyachandran
Assistant Director, Remote
Sensing Applications
Division

Demetrio Zourarakis,
Chair, Region Officers
Council

Hope Morgan,
Chair, Technical Division
Directors Council

Oscar Duran,
Chair, Student Advisory Council

Youssef Kaddoura,
Chair, Early-Career Professionals Council

continued on page 18

Results of the 2023 National Election

• Vice President	Amr Abd-Elrahman	
• Professional Practice Division	Matt Elious	Assistant Director
• Primary Data Acquisition Division	Ravi Soneja	Assistant Director
• Remote Sensing Applications Division	Indu Jeyachandran	Assistant Director

Results of Council Elections

• Region Officers Council	Demetrio Zourarakis	Chair
• Technical Division Directors Council	Hope Morgan	Chair
• Student Advisory Council	Oscar Duran	Chair
• Early-Career Professionals Council	Youssef Kaddoura	Chair

2023 ASPRS Board of Directors

• President	Lorraine Amenda	Term: February 2023 – February 2024
• President-Elect	Bandana Kar	Term: February 2023 – February 2024
• Vice President	Amr Abd-Elrahman	Term: February 2023 – February 2024
• Immediate Past President	Chris Parrish	Term: February 2023 – February 2024
• Student Advisory Council	Oscar Duran	Term: February 2023 – February 2024
• Early Career Professional Council	Youssef Kaddoura	Term: February 2023 – February 2024
• Committee Chairs Council	David Stolarz	Term: February 2022 – February 2024
• Sustaining Members Council	Ryan Bowe	Term: February 2022 – February 2024
• Region Officers Council	Demetrio Zourarakis	Term: February 2023 – February 2025
• Technical Division Directors Council	Hope Morgan	Term: February 2023 – February 2025
• Secretary	Harold Rempel	Appointed
• Treasurer	John McCombs	Appointed
• Executive Director	Karen Schuckman	Appointed

NEW ASPRS MEMBERS

ASPRS would like to welcome the following new members!

Babatunde Aderibigbe
Faiza Ahmed
Opeyemi Emmanuel Alabi
Gunjan Barua
Rebecca Bosworth
Emily M. Brown
Namrata Chatterjee
Janelle Chojnacki
Nathan Drew Comin
Jacob Darrah
Ellen Claudeth Delgado
Liubov Dumarevskaya
Mason Dupre
Bethany N. Ekiss
Gregory Jones Ellsworth
Prof. Peng Fu
Benjamin Hampton
Morgan Harbin
Ngozi Gloria Johnson, PhD
Timothy A. Johnston
Nivedita Priyadarshini Kamaraj
Megan Karczewski
Yunus Kaya, PhD
Minho Kim
Douglas Peter King
Matthew Kratzer
Kelly J. Kriel
David Jonathan Kuxhausen
Wenhao Liu
Ying Lu
Claudia Luna
Mark Martin
Anuska Narayanan
Prof. Uriel Perez
Scott Pieknik
Mashoukur Rahaman
Minoarimanana Ny Aina Rakotoarivony
Alexys Herleym Rodriguez Avellaneda
Batuhan Sariturk
Michael Sentman
Douglas R. Sherrill
Steve Shin
Rakibul Shogib
Hunsoo Song
Jane Southworth, PhD
Ji Won Suh
Scott Vannetta
Casey White
Mimi White
Michael Zarlengo
Jaqueline Zdebski
Adam Zyla

FOR MORE INFORMATION ON ASPRS MEMBERSHIP, VISIT
HTTP://WWW.ASPRS.ORG/JOIN-NOW

Exploring the Addition of Airborne Lidar-DEM and Derived TPI for Urban Land Cover and Land Use Classification and Mapping

Clement E. Akumu and Sam Dennis

Abstract

The classification and mapping accuracy of urban land cover and land use has always been a critical topic and several auxiliary data have been used to improve the classification accuracy. However, to the best of our knowledge, there is limited knowledge of the addition of airborne Light Detection and Ranging (lidar)-Digital Elevation Model (DEM) and Topographic Position Index (TPI) for urban land cover and land use classification and mapping. The aim of this study was to explore the addition of airborne lidar-DEM and derived TPI to reflect data of Landsat Operational Land Imager (OLI) in improving the classification accuracy of urban land cover and land use mapping. Specifically, this study explored the mapping accuracies of urban land cover and land use classifications derived using: 1) standalone Landsat OLI satellite data; 2) Landsat OLI with acquired airborne lidar-DEM; 3) Landsat OLI with TPI; and 4) Landsat OLI with airborne lidar-DEM and derived TPI. The results showed that the addition of airborne lidar-DEM and TPI yielded the best overall urban land cover and land use classification accuracy of about 88%. The findings in this study demonstrated that both lidar-DEM and TPI had a positive impact in improving urban land cover and land use classification.

Introduction

Land cover generally refers to the physical characteristics of the Earth's surface, captured in the distribution of vegetation, soil, water, and other physical features of the Earth, whereas land use is the way in which land has been used by humans and their habitat, usually with an emphasis on the functional role of land for economic activities (Liping *et al.* 2018; McConnell 2015). The understanding of urban land cover and land use is relevant to help project future change in land cover. Furthermore, it provides a pathway to understand the effects of different land management options and feedback to the environment to better manage land resources. Urban land cover and land use maps are generally used to support landscape analyses in the areas of natural and resource management, biodiversity conservation, hydrology and climate modeling, environmental protection, and urban planning (Akumu *et al.* 2018; Parent *et al.* 2015; Yu *et al.* 2014).

Urban land cover and land use information can be easily derived from airborne and satellite data. However, data from Landsat satellite series have been used in more than 40% of research publications relating to land cover classification (Yu *et al.* 2014). The spectral information of satellite remotely sensed data such as Landsat Operational Land Imager (OLI) makes it possible to extract land cover and land use information. This is because different land cover and land use types interact differently with the electromagnetic radiation from sunlight. However, because of the limitation that causes many individual, remotely sensed images to either have high spatial resolution or high spectral resolution, there is a need to explore multi-source data to improve land cover and land use classification.

With the advent and development of airborne Light Detection and Ranging (lidar) data in recent years, there is a need to explore the potential of airborne lidar products and derived topographic metrics such as Digital Elevation Model (DEM) and Topographic Position Index (TPI) in urban land cover and land use classification and mapping. Airborne lidar is a laser probing and scanning technique for bathymetric and topographic applications (Yan *et al.* 2015). It transmits pulses of laser light toward the ground using a scanner mirror. Some of this energy is scattered back towards the aircraft and recorded by the receiving unit. Onboard Global Positioning System and inertial measurement unit document the location X, Y, and elevation Z at the instant the laser pulse is sent and received. Hence, airborne lidar data provides three-dimensional records of the features on the Earth's surface. With a cloud of laser range measurements used to calculate the three-dimensional coordinates of a survey area, a DEM can be effectively generated from airborne lidar data (Sharma *et al.* 2021; Stular *et al.* 2021). Furthermore, the DEM can be used to derive topographic attributes including topographic position index by analyzing change in elevation values within a neighborhood size window. A TPI reflects the difference in elevation between a particular cell and all cells in a neighborhood window (Weiss 2001) A positive value of TPI implies the cell is higher than its surroundings, whereas a negative value infers it is lower than its surroundings. TPI values near zero imply flat areas where the slope is near zero or mid-slope areas (Jenness *et al.* 2013). Hence, TPI compares the elevation of each pixel in a digital elevation model to the mean elevation of the neighborhood and defines landform position class of each pixel. It could be used to delineate landforms such as valleys, plains, and ridges with associated land cover categories.

In recent studies, airborne lidar data have shown some potential in delineating land cover and land use information when used alone or integrated with other multispectral data (Arroyo *et al.* 2010; Im *et al.* 2008; Koetz *et al.* 2008; Miliaresis and Kokkas 2007). For example, Singh *et al.* (2012) explored the integration of airborne lidar structural and intensity surface models with Landsat Thematic Mapper (TM) in urban land cover and land use mapping. They found that the integration of canopy height and digital surface model with Landsat TM increased the total mapping accuracy by about 32% compared to standalone airborne lidar data. Likewise, the mapping accuracy increased by 8% compared to Landsat TM alone at 30 m spatial resolution. Olmanson and Bauer (2017) integrated airborne lidar-DEM with canopy height and Landsat satellite data to map and monitor land cover change between 1990 and 2010. They found about 2% increase in overall land cover classification accuracy when airborne lidar-DEM and canopy height was integrated with Landsat satellite data compared to using Landsat satellite data alone. Furthermore, Matasci *et al.* (2018) combined reflectance data from Landsat TM and Enhanced Thematic

Department of Agricultural and Environmental Sciences, College of Agriculture, Tennessee State University, Nashville, Tenn. 37209 (aclemen1@tnstate.edu).

Contributed by Petra Helmholz, May 27, 2021 (sent for review October 5 2021; reviewed by Fanar M. Abed, Yousif Mousa).

Photogrammetric Engineering & Remote Sensing
Vol. 89, No. 1, January 2023, pp. 19–26.
0099-1112/22/19–26

doi: 10.14358/PERS.21-00029R2

A Machine Learning Method for Building Height Estimation Based on Sentinel-2 Bi-Temporal Images

Zhigang Deng, Xiwei Fan, and Jian Chen

Abstract

Building height information is essential for many applications such as urban planning and population density estimation. The building shadow length varies according to seasons, which is shown as different digital number values in multi-temporal images. Thus, the bi-temporal satellite remote sensing images of Sentinel-2 are used to estimate the buildings height in this study. An area of 15 km × 15 km in Beijing, China is taken as the study area. By preprocessing the data, the remaining pixels are split into two parts: 70% as the training data set and the rest as the testing data set. Then, one classification model and three regression models are proposed with using Random Forest (RF) method. Based on the testing data, it shows that the accuracy rate of the classification model has reached 98.4% with the kappa coefficient of 0.93. And the regression models' root-mean-square error (RMSE) is 0.61 floor for 1–6 floors group, 0.41 floor for 7–12 floor group, and 0.98 floor for above 12 floor group. The final RMSE is 1.62 floor with RF models. In general, this study shows the feasibility of using satellite mid-resolution optical image to estimate the building height and provides an important reference for regional building height estimation in the future.

Introduction

With the rapid development of urbanization, more than half of the world's population lives in cities (Manning 2011). In China, the Seventh National Census data shows that the urbanization rate of the permanent population has reached 63.89% in 2020, an increase of 14.21% from 2010. Moreover, the urbanization process of the permanent population at the developing country such as China has accelerated in the past 10 years. With the continuous progress of urbanization, the cities tend to become taller beside grow larger. Thus, we not only need to obtain two-dimensional information of the city areas, but also the three-dimensional (3D) spatial information. Apart from this, building height information is related to the urban heat island effect (Li *et al.* 2022; Wang *et al.* 2020), city climate at the local scale (Cao *et al.* 2021), population distribution at the spatial and temporal dimensions (Alahmadi *et al.* 2013; Leichtle *et al.* 2019), and so on. More importantly, it is also a key reference for urban functional zone planning and disaster emergency rescue.

Compared with the traditional field investment method, the remote sensing technology is a more efficient way to acquire building height information at large scales. To acquire buildings height based on remote sensing data, one typical group of methods is using the geometric relationship between building height and the corresponding shadow cast on ground in very-high-resolution (VHR) optical images (Cheng *et al.* 2007; Shao *et al.* 2011; Wang *et al.* 2014). However, in actual applications, those methods were restricted due to the overlapping of shadows from different buildings, and the complex shapes of the buildings, and topographic relief, etc. (Biljecki *et al.* 2017). In addition, the relatively high cost of VHR optical images is also limiting the popularization of those method. Especially for most developing countries, where buildings updated more frequently, low cost, or open access remote sensing images are more practical (Gong *et al.* 2011; Li *et al.* 2016). With the development of interferometric synthetic aperture radar (InSAR) technology, the digital surface model (DSM) data can be acquired based on satellite InSAR data. Then the building height information is extracted based on the mask algorithm on DSM (Dubois *et al.* 2016; Gamba *et al.* 2000; Stilla *et al.* 2003; Wegner *et al.* 2014). However, the noise characteristics (Stilla *et al.* 2003) and the signal is easily affected (Thiele *et al.* 2007) in InSAR technology.

In addition to the traditional visible and synthetic aperture radar (SAR) satellite remote sensing images, some new method, such as photogrammetric method based on stereo image pairs, light detection and ranging (lidar) data acquired on manned or unmanned airborne platforms were used to determine the building height and construct the 3D model of city areas. The vertical or slant view images commonly acquired by drone with a relatively high overlap rate can be used to obtain city scale 3D models based on some photogrammetric software (Martinez-Carricondo *et al.* 2020; Svennevig *et al.* 2015; Trekin *et al.* 2020). While the lidar instrument uses the principle of laser ranging to obtain the 3D coordinates, reflectivity and texture information of the building surface is used to construct the building's 3D model (Ergun 2007; Yu *et al.* 2018; Zhu and Ma 2014). Using these technical, it is possible to obtain building height information with a high accuracy, but the processing of images takes a long time, and it is difficult to reconstruct the building height at regional or global scale using airborne remote sensing data.

Apart from the data sources, with the development of machine learning technique in recent years, some Artificial Neural Networks (ANN), Random Forests (RF), and Support Vector Machines (SVM) have been widely used for building height estimation. For example, based on the dual-polarization information index in the Sentinel-1 SAR data (Torres *et al.* 2012), and Li *et al.* (2020) used the RF method to study the height of buildings at 500 m resolution in seven major cities in the United States. Further, Frantza *et al.* (2021) combined *Sentinel-1A/B* and *Sentinel-2A/B* time series to map building heights for entire Germany based on SVM and RF models. Recently, deep learning made major advances in solving problems in many domains (LeCun *et al.* 2015). In building height extraction, Cao *et al.* (2021) propose a multispectral, multi-view, and multi-task deep network (called M^{3}Net) for

Zhigang Deng and Xiwei Fan are with Key Laboratory of Seismic and Volcanic Hazards, China Earthquake Administration, Beijing 100029, China (Corresponding author: Fanxiwei@ies.ac.cn).

Zhigang Deng and Xiwei Fan are also with the Institute of Geology, China Earthquake Administration, Beijing 100029, China.

Zhigang Deng and Jian Chen are with the School of Engineering and Technology, China University of Geosciences Beijing, Beijing 100083, China.

Contributed by Ahmed Abd El-Latif, February 18, 2022 (sent for review July 18, 2022; reviewed by Bruno Vallet, Salman Ahmadi).

Photogrammetric Engineering & Remote Sensing
Vol. 89, No. 1, January 2023, pp. 27–36.
0099-1112/22/27–36

doi: 10.14358/PERS.22-00054R2

Generation of High-Resolution Orthomosaics from Historical Aerial Photographs Using Structure-from-Motion and Lidar Data

Ji Won Suh and William Ouimet

Abstract

This study presents a method to generate historical orthomosaics using Structure-from-Motion (SfM) photogrammetry, historical aerial photographs, and lidar data, and then analyzes the horizontal accuracy and factors that can affect the quality of historical orthoimagery products made with these approaches. Two sets of historical aerial photographs (1934 and 1951) were analyzed, focused on the town of Woodstock in Connecticut, U.S.A. Ground control points (GCPs) for georeferencing were obtained by overlaying multiple data sets, including lidar elevation data and derivative hillshades, and recent orthoimagery. Root-Mean-Square Error values of check points (CPs) for 1934 and 1951 orthomosaics without extreme outliers are 0.83 m and 1.37 m, respectively. Results indicate that orthomosaics can be used for standard mapping and geographic information systems (GIS) work according to the ASPRS 1990 accuracy standard. In addition, results emphasize that three main factors can affect the horizontal accuracy of orthomosaics: (1) types of CPs, (2) the number of tied photos, and (3) terrain.

Introduction

Land use land cover (LULC) change plays a fundamental role in recording the impact of human activities on earth surface processes and understanding these impacts is one of the grand challenges in environmental science today (National Research Council 2001). Satellite-based data such as Landsat have been widely used to understand LULC in the field of remote sensing (Leh *et al.* 2013; Verbesselt *et al.* 2012; Zhu *et al.* 2016, 2020; Zhu and Woodcock 2014), but are limited in terms of temporal scope (Landsat first launched in 1972) and spatial resolution (with the best available pixel resolution being 15–30 m between the 1970s and early 2000s). To understand historical LULC changes prior to the satellite era and at much higher spatial resolution, historical aerial photography has long been considered an important source of data, adding multiple new time intervals in the study of land use activity in forestry, ecology, urban planning, cultural resources, and geomorphology related studies (Kadmon and Harari-Kremer 1999; Llena *et al.* 2018; Mallinis *et al.* 2011; Nita *et al.* 2018; Rocchini *et al.* 2006; Sevara 2013; Verhoeven *et al.* 2012; Zomeni *et al.* 2008).

Unlike modern remote sensing imagery derived from airplanes, unmanned aerial vehicles (UAV) or satellites, a number of issues need to be taken into account when using historical aerial photographs. These include: (1) low data accessibility, (2) no georeferencing, (3) time-consuming work for mosaicking fragmented aerial photograph campaigns and scaling up the spatial extent, (4) poor information for aligning or calibrating individual aerial photograph such as camera position, flight altitude, yaw, pitch, and roll (Fox and Cziferszky 2008; Frankl *et al.* 2015), (5) no ground control points (GCPs), which are crucial in removing inherent radial distortion and tilt for georeferencing (Bolstad 1992; Wolf *et al.* 2014), and (6) low image quality due to digital scanning. These problems have generally restricted the application of modern photogrammetric techniques when dealing with historical data (Lingua *et al.* 2009; Turner *et al.* 2012; Weng *et al.* 2013). In addition, they can attenuate errors associated with automated image processing in photogrammetric software such as Agisoft Metashape and Pix4Dmapper when it comes to the shortage of metadata or increasing the number of photos stitched.

Despite these challenges, a number of studies have been conducted to orthorectify historical aerial photographs and reconstruct historical digital elevation models (hDEM) based on photogrammetric techniques such as Structure-from-Motion (SfM). The historical aerial photography considered in these studies ranges from the 1930s (Fox and Cziferszky 2008; Frankl *et al.* 2015; Geyman *et al.* 2022) to the 1990s (Arnaud *et al.* 2015) and most of the research has been concentrated on images from the 1950s onward (Comiti *et al.* 2011; Gennaretti *et al.* 2011; Gomez 2014; Kadmon and Harari-Kremer 1999; Llena *et al.* 2018; Marignani *et al.* 2008; Maurer and Rupper 2015; Nebiker *et al.* 2014; Rocchini *et al.* 2006). To overcome the lack of external information of historical data, creating GCPs from reference data such as DEMs is essential during SfM processing. Depending on the spatial resolution of reference data, the quality of output orthomosaics or DEMs varies. The quality of orthomosaics has been evaluated by root-mean-square error (RMSE) and the RMSE results with coarse reference data (e.g., ~10–40 m) ranges from 5 m to 15 m (Baker *et al.* 1995; Gennaretti *et al.* 2011; Marignani *et al.* 2008; Rocchini *et al.* 2006).

The advent of Light Detection and Ranging (lidar) data and high-resolution DEMs (e.g., 1 m) can lead to increasing the accuracy of historical orthomosaics and hDEMs given that lidar derivatives such as hillshades allow for visualizing of small-scale features and greater potential for choosing GCP with accurate coordinates and elevation values. To date, however, the application of high-resolution topographic data from lidar in SfM photogrammetry processing has been focused on assessing vertical accuracy of hDEM products (Child *et al.* 2021; Nebiker *et al.* 2014) rather than extracting GCPs for the orthomosaic. One of reasons for this is that high-resolution historical imagery needs high-resolution topographic data as a reference to build orthomosaics with less horizontal error. Furthermore, there is a lack of research focused on expanding the spatial extent of orthophotos made from high-resolution historical aerial photos (i.e., less than 1:20 000 scale, less than 1m pixel resolution) and lidar data. This is because a large number of historical photos need to be aligned and orthomosaicked to cover larger spatial extent, in contrast to the aforementioned previous studies that use less than 40 photos. In other words, the paucity of such studies underlines the need for an improved methodological approach. Lidar data and its derivatives provide an opportunity to fill in the gap between the low resolution of reference topographic data (e.g., 30 m DEMs) and the resolution of input from historical imagery (e.g., 1 m) (Llena *et al.* 2018).

Ji Won Suh and William Ouimet are with the Department of Geography, University of Connecticut, Storrs, CT 06269 (ji.suh@uconn.edu).

William Ouimet is also with the Department of Earth Sciences, University of Connecticut, Storrs, CT 06269.

Contributed by Dorota Iwaszczuk, March 17, 2022 (sent for review May 6, 2022; reviewed by Michael Cramer).

Photogrammetric Engineering & Remote Sensing
Vol. 89, No. 1, January 2023, pp. 37–46.
0099-1112/22/37–46

doi: 10.14358/PERS.22-00063R2

The goal of this paper is to present the generation of high-resolution historical orthomosaic over a broad area using SfM photogrammetry combined with GCPs from lidar derivatives. Our objectives are to (1) provide a method to build high-resolution historical orthomosaics by using 1934 and 1951 black and white aerial photographs focused on the town of Woodstock, Connecticut, United States; (2) evaluate the horizontal accuracy of orthomosaics based on RMSE values for overall assessment and residual error to understand spatial distribution of errors, and (3) analyze factors that can affect the quality of these historical orthophotos by comparing orthomosaics from 1934 and 1951.

Data and Methods

Study Area

This study was conducted focusing on the town of Woodstock in northeastern Connecticut. In order to cover the entirety of Woodstock, our study area is a rectangle and includes adjacent towns described in Figure 1. To be specific, Figure 1B shows the DEM ranging from 64 m to 335 m and topography in the west part comprised mainly of hilly uplands with mixed coniferous-deciduous forests and agricultural lands. On the other hand, the east part consists of lowland used for agricultural lands as well as mixed forests and muddy brook which flows south into Roseland lake. Distributed over the entire study area are stone walls, stacked around agricultural lands that indicate an anthropogenic legacy of English-style agriculture during the 17th to 20th centuries (Cronon 1983; Thorson 2002) (Figure 1C and 1D). They are easily detected in a hillshade map derived from lidar in open area and deciduous forest (Johnson and Ouimet 2014, 2016).

Data

Collected data for this study can be divided into two sets in terms of usages: to produce historical orthomosaics and to create GCPs (Table 1). In particular, the first data set includes high-resolution black and white air photos of 1934 and 1951 provided from the Connecticut State Library (1934, 1951). For 1934, 141 air photos (spatial scale 1:12 000) were used for an orthomosaic covering about 264 Km² area. The

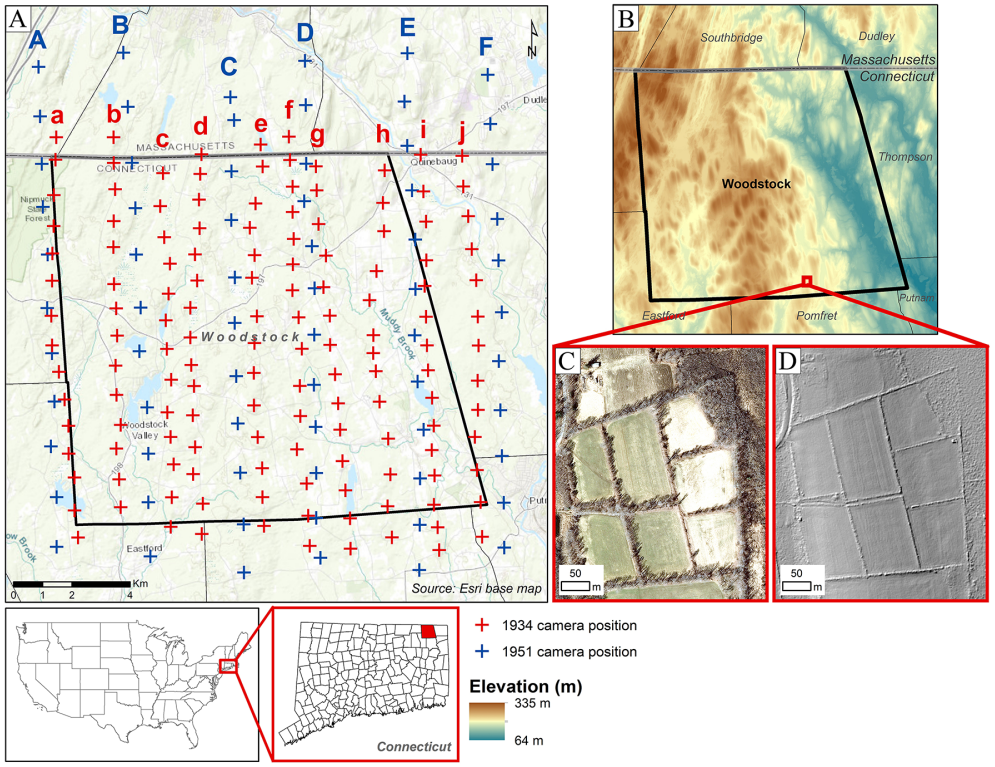

Figure 1. Map of the study area. (A) study area with camera positions of 1934 and 1951 aerial photographs (ESRI, 2012). Lower case and upper case refer to 1934 and 1951 north-south flight paths, respectively; (B) Digital Elevation Model ranging from 64 m to 335 m; (C) an example of stone walls with 2012 leaf-off orthophoto (CT ECO 2012); (D) an example of stone walls with a hillshade map derived from lidar.

Table 1. List of maps and aerial photographs used for this study.

Data Usage	Data Type	Year	Date	Resolution/Map Scale	# of Images (Covering Area)	Source
Historical orthomosaics	A/BW	1934	April 1934	1:12 000	141 (264 Km²)	Connecticut State Library[1]
	A/BW	1951	5 September 1951 13 October 1951 25 November 1951 27 November 1951	1:20 000	68 (380 Km²)	Connecticut State Library[2]
Reference data	A/O/C	2012		0.3 m		CT ECO
	A/O/C	2016		0.07 m		CT ECO
	DEM	2016		1 m		CT ECO
	Hillshade	2016		1 m		2016 DEM

A: aerial photographs; O: ortho-rectified aerial photographs; BW: black and white; C: color. CT ECO = Connecticut Environmental Conditions Online; DEM = digital elevation model.

[1] Connecticut State Library, 1934 Aerial Surveys, Record Group 089:011, Department of Transportation, State Archives.

[2] Connecticut State Library, 1951 Aerial Surveys, Record Group 089:011b, Department of Transportation, State Archives.

vertical photography was taken in April 1934 (note that specific dates were not available) by Fairchild Aerial Survey Corporation using a K-3 aerial survey camera with a 241.3 mm focal length. The survey flights were flown at an altitude of around 3500 m. The overlap rate between two images were approximately 50%. This historical photography was digital-scanned as a 1270 dots-per-inch in 2006. On the other hand, 68 air photos of 1951 (spatial scale 1:20 000) were used covering about 380 Km². Robinson Aerial Surveys took 1951 imagery on the following dates: 5 September 1951, 13 October 1951, 25 November 1951, and 27 November 1951. Unlike 1934 photography, detailed information about survey and scanning process for 1951 was not available. Regarding the number of photos of 1934 and 1951, each 1934 photo covers small extent compared to 1951 photo so that the more photos of 1934 were collected.

As reference data to create GCPs, the second data set includes recent orthophotos (2012 and 2016), DEM derived from 2016 lidar, and a hillshade map produced from lidar DEM. First, 2012 and 2016 high-resolution orthophotos were streamed from Connecticut Environmental Conditions Online (CT ECO) image services in ArcGIS Desktop 10.5 (CRCoG 2016; CT ECO 2012). The spatial resolution of 2012 and 2016 orthoimagery is 0.3 m and 0.07 m, respectively (Table 1). Next, high-resolution DEM from lidar is used to get elevation values of GCPs with fewer errors. Lastly, lidar DEM is also a source to produce a hillshade map that is able to detect surface features such as stone walls (Johnson and Ouimet 2014), which ensures the horizontal position of target locations.

A Workflow for Generating Historical Orthomosaics

In order to build 1934 and 1951 historical orthomosaics and conduct horizontal accuracy assessment, we provided a workflow from steps 1 through 11 by using Agisoft Metashape 1.6 and ArcGIS Desktop 10.5, described in Figure 2. Agisoft LLC (2019) provides a general workflow to build an orthomosaic or DEMs and a number of studies have followed it (Ajayi *et al.* 2017; Midgley and Tonkin 2017; Nita *et al.* 2018; Riquelme *et al.* 2019). However, it needs to be improved for applications involving historical data in order to overcome a lack of photo information and build high-quality georeferenced orthophotos that can be used for mapping and GIS purposes. A workflow consists of three general stages, (1) preprocessing (steps 1 and 2), (2) georeferencing and orthomosaicking (steps 3 to 10), and (3) horizontal accuracy assessment (step 11). Details on each step will be addressed in the following sub-sections: "Pre-Processing Stage (Steps 1 to 2)", "Photo-Alignment/Orthomosaicking Stage (Steps 3 to 10)", and "Horizontal Accuracy Assessment Stage (Step 11)". The data were processed with Intel Xeon CPU E5-2687W v3 at 3.10 GHz with 10-core, 128 GB RAM, 20 processors, AMD FirePro W7100 graphics card, and operating on Windows 10 64-bit.

Pre-Processing Stage (Steps 1 to 2)

As a preprocessing stage, input historical photos were masked (step 1) to eliminate unnecessary information such as frame and letters and then the image quality of these photos was estimated (step 2) based on the sharpness value of images that Agisoft image quality tool provides (Agisoft LLC 2019). A blurry image can reduce an orthophoto quality at the final step so images below 0.5 sharpness value out of 1.0 were discarded during the orthomosaicking process (step 10 in Figure 2). The quality test result of 1934 air photos ranges from 0.47 to 0.66 and two photos below the 0.5 quality threshold were disabled. Figure 3 represents an image quality comparison between 0.47 (A) and 0.66 (B) snapped in the same spatial extent. On the other hand, all 1951 air photos were used since they meet the requirement by ranging between 0.74 and 0.88.

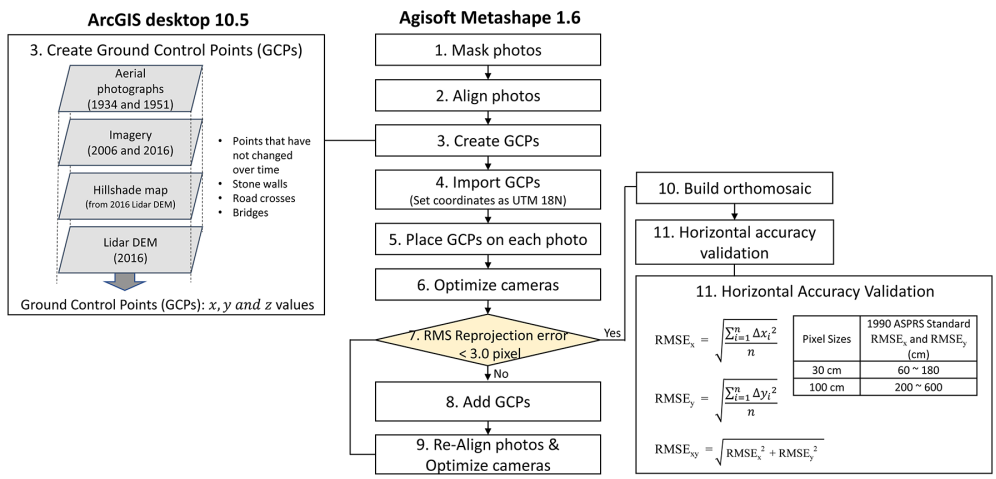

Figure 2. A flowchart for generating orthomosaics of historical aerial photographs using Agisoft Metashape and ArcGIS desktop. DEM = digital elevation model; RMSE = root-mean-square error.

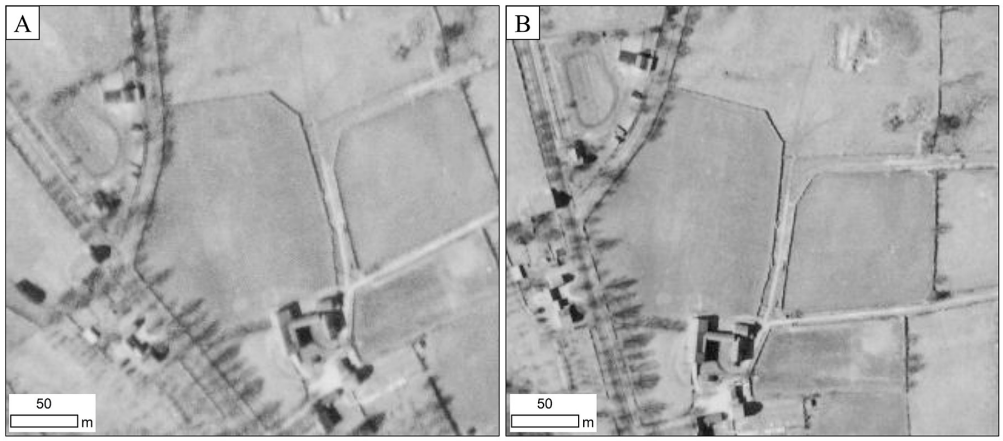

Figure 3. An image quality comparison between 0.50 (A) and 0.61 (B) snapped from 1934 air photos in the same spatial extent. 1934 Aerial Surveys, State Archives Record Group 089:011, State Archives, Connecticut State Library.

Photo-Alignment/Orthomosaicking Stage (Steps 3 to 10)

In this stage, photo-alignment (step 3) was conducted with high accuracy and the generic pair preselection option in Agisoft Metashape. The key point limit and tie point limit was set as 100 000 and 8000, respectively. Given that no information about camera position is used during the photo-alignment process, GCPs with northing, easting, and elevation values should be placed on photos to better alignment as well as georeferencing.

However, there are no GCPs available for historical data, so we defined GCPs (step 4) by selecting points that have not changed over time in a comparison of historical air photos, recent orthophotos, and lidar hillshade maps. Three aspects were taken into account when selecting GCPs. First, the priority of point selection was set considering frequency and stability of features through time. Therefore, stone walls were the first priority since they existed in the entire study area and were relatively stationary features pre-1934. Then it is followed by road crosses or edges, fixed structures (e.g., bridge, dam, etc.), and the attributes of natural landscape (e.g., creek crosses) (Figure 4). However, the attributes of natural landscape such as creek crosses can be relatively easily changed over time so it was only considered for GCP selection when the rest of potential features (e.g., stone walls, road crosses or edges, fixed structures) were unavailable.

The second aspect was the distribution of GCPs. Given that GCPs with three-dimensional (3D) coordinates strongly control error behavior (Wolf *et al.* 2014), the optimal distribution of GCPs is a point on each corner and additional points uniformly and densely distributed

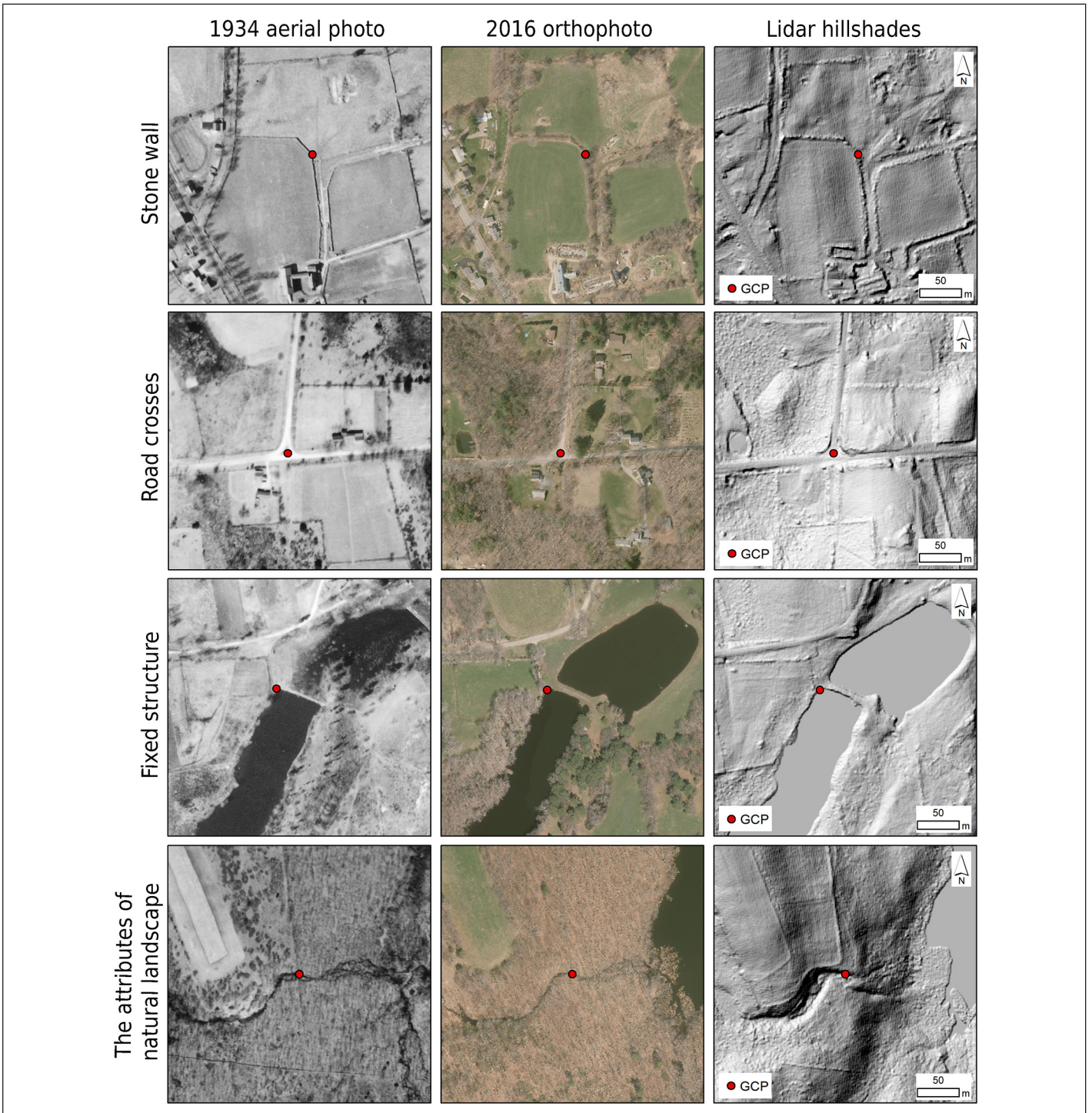

Figure 4. Examples of ground control points (GCPs) on 1934 aerial photo, 2016 orthophoto, and lidar hillshade. 1934 images from 1934 Aerial Surveys, State Archives Record Group 089:011, State Archives, Connecticut State Library.

throughout an image. We tried to place our GCPs as uniformly as possible but were limited by the fact that landscape changes between the images used are often not uniform. When using historical aerial photograph, with 50–90 years between original images and modern lidar and orthophoto data sets, this will likely also be a limitation contributing to error.

The last aspect was the number of photos that each GCP stitched. Each GCP should be located in the place where at least two photos were overlapped. Once GCPs are created at least 1:500 scale level through ArcGIS desktop, northing and easting values were extracted from created GCPs, and elevation values were extracted from lidar DEM (Llena *et al.* 2018) and exported as CSV format, herein we used UTM 18N projection (EPSG: 6347) since measuring horizontal distances was required in accuracy assessment (step 11). After creating GCPs, these GCPs were imported in Agisoft and placed on photos (step 5).

Steps 6 to 9 were repeated until RMS reprojection error was less than 3.0 pixels (see step 7). Camera optimization (step 6) was undertaken using Brown's distortion model (Agisoft LLC 2019) to adjust photo-alignment considering lens distortion. In particular, the following 11 variables were used; focal length (f), principal point offset (c_x and c_y), radial distortion coefficients (K_1, K_2, K_3, and K_4), affinity and skew transformation coefficients (B_1 and B_2), and tangential distortion coefficients (P_1 and P_2). This was an alternative way to overcome a lack of camera calibration information for historical imagery. The quality of photo alignment step is evaluated by RMS reprojection error (in pixel) that is a geometric error associated to the distance between a reconstructed 3D point and an original 3D point detected on the photo. If RMS reprojection error was greater than 3.0 pixel, more GCPs were created and placed on photo. If RMS reprojection error was less than 3.0 pixel, building an orthomosaic (step 10) was conducted. As stated in the description of step 2, images above 0.5 quality threshold were used during an orthomosaicking step and surface parameter was set as 1 m resolution lidar DEM instead of hDEM derived in Metashape due to low resolution of hDEM (e.g., 40 m). Then the orthophoto product was exported and assessed for horizontal accuracy (step 11).

Horizontal Accuracy Assessment Stage (Step 11)

To assess horizontal accuracy of the 1934 and 1951 orthophotos, check points (CPs) were placed on the photo to calculate the residual error of each point and the standard deviation of all residual errors (RMSE). Like GCPs, CPs were typically one of four types: (1) stone walls (SW), (2) road crosses and edges (Rd), (3) natural landscape feature (NL) (e.g., creek crosses), and (4) fixed structures (FS) (e.g., bridge, dam, etc.). In general, RMSE values (i.e., $RMSE_x$, $RMSE_y$, and $RMSE_{xy}$) of CPs are widely used to evaluate the quality of an orthophoto product (American Society for Photogrammetry and Remote Sensing 1990, 2014; Congalton and Green 2009; Tomaštík *et al.* 2019) since they are not used during photo-alignment process. In this study, they are calculated as:

$$\mathrm{RMSE}_x(m) = \sqrt{\frac{\sum_{i=1}^{n}(x_i - \hat{x}_i)}{n}} \quad (1)$$

$$\mathrm{RMSE}_y(m) = \sqrt{\frac{\sum_{i=1}^{n}(y_i - \hat{y}_i)}{n}} \quad (2)$$

$$\mathrm{RMSE}_{xy}(m) = \sqrt{\mathrm{RMSE}_x^{\,2} + \mathrm{RMSE}_y^{\,2}} \quad (3)$$

where:

x_i is the easting value of CPs from a lidar hillshade map; $\hat{x}_i$ is the estimated easting value of CPs in an orthomosaic product; y_i is the northing value of CPs from a lidar hillshade map; and $\hat{y}_i$ is the estimated northing value of CPs in an orthomosaic product.

The results of RMSE values were compared to American Society for Photogrammetry and Remote Sensing (ASPRS) 1990 standard shown in Table 2. Even though the 1990 standard is regarded as a legacy, we used this standard instead of the recent RMSE standard (e.g., less than 1.4 cm * resolution of geospatial data) given that our inputs were 1934 and 1951 historical data.

Table 2. ASPRS 1990 horizontal accuracy standard information including classes, RMSE values, and recommended uses for each class.

	1990 Standard $RMSE_x$ and $RMSE_y$ (m) based on pixel size		
Class	**1934**	**1951**	**Recommended Use**
1	0.6 m	2.0 m	Highest accuracy work
2	1.2 m	4.0 m	Standard mapping and GIS work
3	1.8 m	6.0 m	Visualization

ASPRS = American Society for Photogrammetry and Remote Sensing; RMSE = root-mean-square error; GIS = geographic information systems.

Results

By following all steps provided in the orthomosaicking workflow (Figure 2), two sets of historical orthomosaics were produced. One is 1934 orthoimage (ground resolution: 0.3 m/pixel) mosaicked with 141 photos covering 264 km² and the other is 1951 orthomosaic (ground resolution: 0.9 m/pixel) stitched with 68 photos covering 380 km². To meet RMS reprojection error condition (<3.0 pixel), 237 of GCPs was used for 1934 and 234 of GCPs was used for 1951. During the photo-alignment step, the total number of valid tie points for 1934 was 185 293 out of 474 139 and the RMS reprojection error was 2.93 pixel. After bundle adjustment, the mean residual errors of X, Y, Z, and total three coordinates for 1934 were 1.15 m, 1.26 m, 5.56 m, and 5.82 m, respectively. For 1951, the total number of valid tie points was 221 475 out of 464 127 and the RMS reprojection error of 1951 point cloud was 1.1 pixel. After bundle adjustment, the mean residual errors of X, Y, Z, and total three coordinates were 1.59 m, 1.54, 9.2 m, and 9.46 m. The bundle adjustment result shows that a large residual error in vertical value (Z) occurred compared to horizontal value (X and Y). This result supports the use of high-resolution lidar DEM as a better resource for the orthomosaicking process instead of the hDEM reconstructed from the historical aerial photographs.

Table 3 and Table 4 shows estimated distance and overlap information for the 1934 and 1951 results based on the estimated camera position by Metashape. The range of side overlap slightly changes depending on the north-south flight path; overall, the survey was flown as regular.

Table 3. Distance and overlap information between camera flight paths of 1934 aerial photographs. The lower case refers to the north-south flight path IDs shown in Figure 1.

1934 Camera Paths	**a–b**	**b–c**	**c–d**	**d–e**	**e–f**	**f–g**	**g–h**	**h–i**	**i–j**
Avg. overlap (km)	1.8	1.7	1.1	2.1	1.4	1.1	1.8	1.7	1.6
Max. overlap (km)	2	1.8	1.3	2.2	1.7	1.4	2.3	1.9	1.9
Min. overlap (km)	1.6	1.6	0.9	2	1	0.8	1.4	1.5	1.2
Side overlap (%)	35–47	35–40	54–67	27–35	41–62	51–73	24–55	45–37	41–60
Forward overlap (%)	45–60								

Table 4. Distance and overlap information between camera flight paths of 1951 aerial photographs. The upper case refers to the north-south flight path IDs shown in Figure 1.

1951 Camera Paths	**A–B**	**B–C**	**C–D**	**D–E**	**E–F**
Avg. overlap (km)	3.35	3.66	2.98	3.71	3.98
Min. overlap (km)	2.9	3.15	2.49	3.38	2.83
Max. overlap (km)	3.13	3.37	2.67	3.53	3.05
Side overlap (%)	28–33	21–25	39–40	19–25	29–36
Forward overlap (%)	60–80				

Horizontal accuracy assessment was then conducted to validate the quality of final orthophoto products by using RMSE values. To do this, a total of 287 CPs for the 1934 orthomosaic and 182 CPs for the 1951 orthomosaic were established for the accuracy evaluation. More CPs for the 1934 orthomosaic were required compared to those for the 1951 orthomosaic due to the number of CPs per image. In addition, the 1951 aerial photographs were taken during leaf-on conditions, which led to additional challenges associated with identifying reference objects that have not changed over and were not forested.

Table 5. RMSE results of 1934 and 1951 orthomosaics. *n* is the number of CPs.

	1934	1951
n	287	182
$RMSE_x$ (m)	0.94	1.28
$RMSE_y$ (m)	1.08	1.28
$RMSE_{xy}$ (m)	1.43	1.82
$RMSE_{xy}$ (m) without extreme outliers (>3 m)	0.83 (*n* = 277)	1.37 (*n* = 173)

RMSE = root-mean-square error; CPs = check points.

RMSE Results of 1934 and 1951 Orthomosaics

Table 5 shows the RMSE results of the 1934 and 1951 orthomosaics. According to the 1990 ASPRS horizontal accuracy standard (Table 2), the 1934 orthomosaic can be used for standard mapping and GIS work in that the RMSE result without outliers is less than 1.2 m and 1951 orthophoto products can be used for highest accuracy work considering the RMSE without outliers is less than 2.0 m (Table 5). It was found that high-resolution historical orthomosaics can be constructed to town-scale with high accuracy and the orthomosaic procedure can be further applied to expand the spatial scale of study area (i.e., state-scale).

Spatial Pattern of Residual Errors

Figure 5 shows the spatial distribution of residual errors of CPs regarding their location: inside and margin area. Figure 6 shows the residual error boxplots of each CPs for inside area and margin area in both 1934 and 1951 orthophoto results. The results demonstrate that (1) the mean residual errors of 1951 orthophoto are larger than those of 1934 orthoimage and this is caused by spatial resolution differences between two periods, (2) the residual errors from the margin area are larger than those from inside area, and (3) extreme outliers tend to be observed in edge part of the margin area. These results of (2) and (3) supported an edge effect reported in previous studies (Hung *et al.* 2019; Khan and Miklavcic 2019; Nogueira and Roberto 2017). It is partly due to the

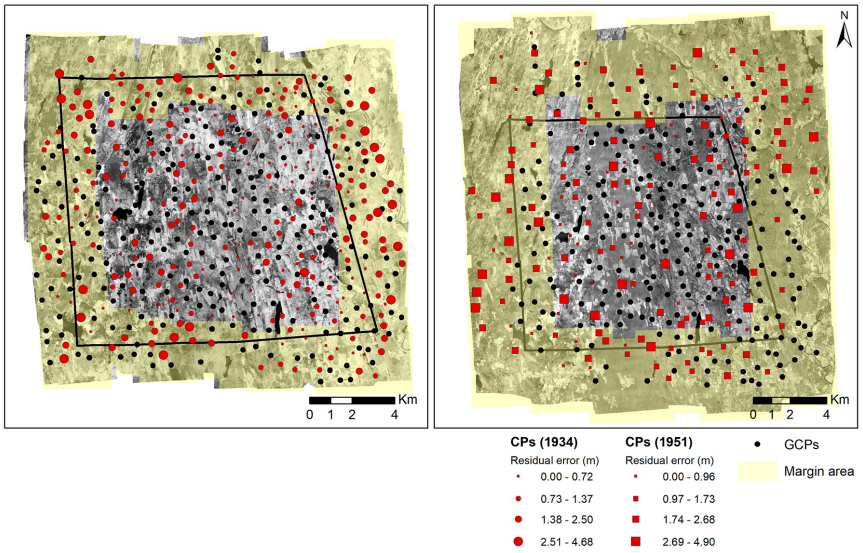

Figure 5. Spatial distribution of residual error from orthomosaic results (A: 1934; B: 1951). CPs = check points; GCPs = ground control points. 1934 Aerial Surveys, State Archives Record Group 089:011, and 1951 Aerial Surveys, State Archives Record Group 089:11b, State Archives, Connecticut State Library.

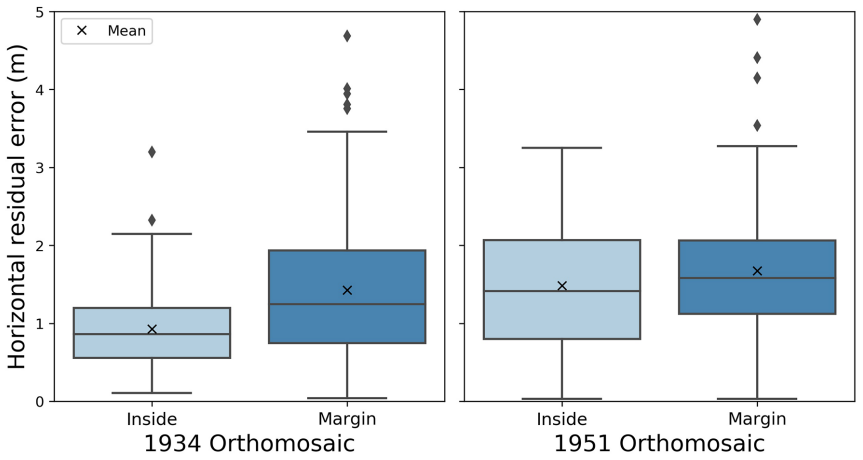

Figure 6. Boxplots of horizontal residual error (m) for inside area and margin area in 1934 (left), 1951 (right). (Ground resolution: 1934 orthomosaic (0.3 m/pixel) and 1951 orthomosaic (0.9 m/pixel)).

fact that the smaller number of key points were extracted and matched from limited images (e.g., two photos) in the margin area.

Discussion

As stated earlier, it was found that the accuracy of a historical orthomosaic can be affected by the spatial resolution of input photos and reference data, and their location (i.e., inside/margin). In other words, the conditions for obtaining high quality of orthomosaics are (1) to use high-resolution input photos (American Society for Photogrammetry and Remote Sensing 2014), (2) to extract reference points from high-resolution reference data such as lidar DEMs and hillshade, and (3) to use additional input photos by buffering a target area at least one flight strip surrounding it to minimize edge effect. However, the results (Figure 5) also demonstrate that a couple of major residual errors occur locally unlike an orthomosaics derived from modern UAV such as a drone. Therefore, we herein discussed additional factors influencing the quality of an orthomosaic from historical aerial photos over a broad area based on a spatial join between CPs' residual errors and map of each factor.

Types of CPs

As aforementioned in section "Horizontal Accuracy Assessment Stage (Step 11)", CPs fall into four types: SW, Rd, NL, and FS. The number of CPs categorized as SW or Rd accounts for ~80% since their locations are relatively easy to be identified between orthomosaic and lidar hillshade and are common landscape features that are static over time. The occurrence of each CP was the close to the same for each time frame: for the 1934 orthomosaic, the number of CPs categorized as SW accounts for 56%, Rd is 22%, NL is 17%, and FS is 5%; for the 1951 orthomosaic, SW accounts for 53%, Rd is 24%, NL is 19% and FS is 4%. Figure 7 is a boxplot representing the distribution of residual error for each type of CP. CPs of SW and Rd are widely distributed throughout the orthomosaics and tend to show lower residual error compared to NL and FS—although it is difficult to generalize this result because the number of points for each type varies and the accuracy may depend on the location of points (e.g., inside/margin area). In addition, SW and Rd types were easily detectable and more easily delineated on the hillshade maps derived from high-resolution lidar DEM.

The Number of Tied Photos

The number of tied photos was considered as a second factor affecting the quality of orthomosaic because, theoretically, the more photos tied to specific reference points, the higher the accuracy of projected point placement (Agisoft LLC 2019). Figure 8 shows boxplots of CPs' residual errors according to the number of tied photos in 1934 and 1951 orthomosaics. Our results do not completely support the theoretical assumption. In the 1934 orthomosaic, mean residual error tends to decrease as the number of tied photos goes from 1 to 5, but in the 1951 orthomosaic, mean residual error does not decrease as the number of tied photos increases. This is likely due to the fact that it is difficult to place reference points in the exact same location in all photos because some photos have poor sharpness or bad conditions.

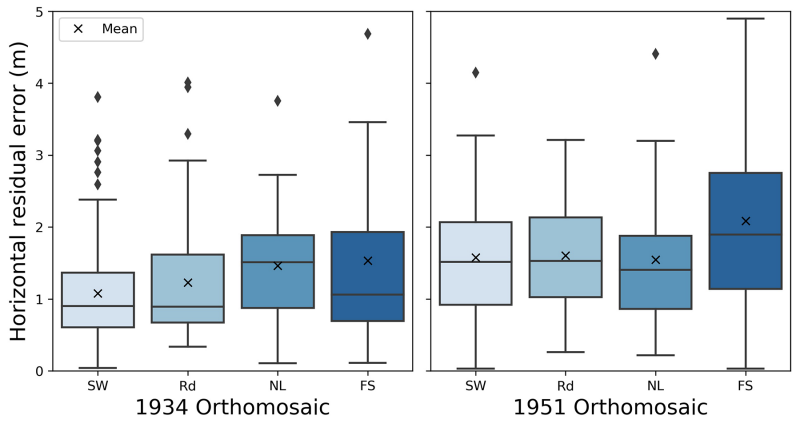

Figure 7. Residual error boxplots of four types of CPs in 1934 (left), 1951 (right). (SW = stone walls, Rd = road crosses or edges, NL = natural landscape features such as creek intersections, FS = fixed structures such as dams or bridges). (Ground resolution: 1934 orthomosaic (0.3 m/pixel) and 1951 orthomosaic (0.9 m/pixel).)

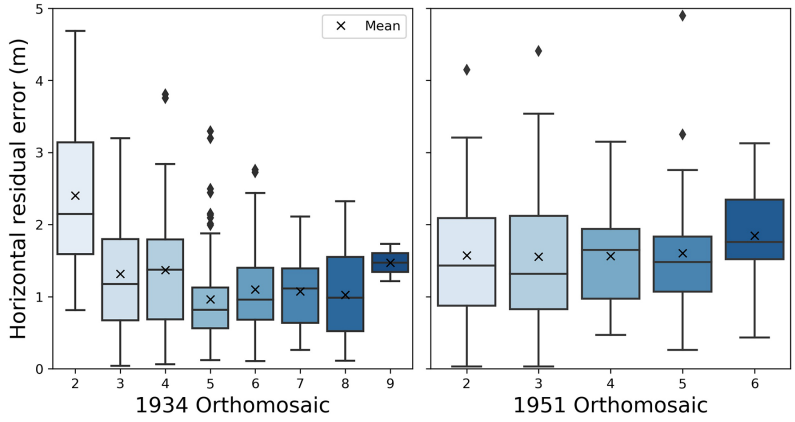

Figure 8. Residual error boxplots as a function of the number of tied photos used in 1934 (left) and 1951 (right). (Ground resolution: 1934 orthomosaic (0.3 m/pixel) and 1951 orthomosaic (0.9 m/pixel).)

Terrain

As the last factor that affects the accuracy of an orthomosaic result, three terrain elements (elevation, relief, and slope) were taken into account (Figure 9). Relief indicates the topographic range in elevation that exists over a specified window; we used a window size of 100 m. Elevation in the study area ranges from 64 m to 335 m, relief ranges from 0 to 71 m, and slope ranges between 0 to 40 degrees. From the perspective of spatial variation, the northwest portion of the study area shows the highest elevation, relief, and slope values. To figure out the relationship between terrain elements and positional accuracy of orthomosaic, each terrain element was reclassified into three classes, which are low (1), medium (2), and high (3) based on natural break and residual error boxplots of terrain conditions were created for both the 1934 and 1951 orthomosaic (Figure 10).

Mean positional residual error of historical orthomosaics increases slightly in areas characterized by higher elevations and higher slope values (Figure 10). One factor contributing to this trend is that fewer GCPs were used in areas with higher elevations and slope values because these areas tend to have high forest cover in our study area, which poses a challenge to identifying GCPs in lidar hillshades and historical aerial photographs. Therefore, it could be the coupling of terrain characteristics with vegetation differences, rather than strictly terrain, that prevents accurate matching of key points in the aerial photos and leads to larger residual errors.

Conclusion

This study presents a methodological procedure for generating high-resolution historical orthomosaic over a broad area using SfM software Agisoft Metashape and ArcGIS desktop, which allows for the incorporation of lidar data. Among 11 steps in the procedure, creating GCPs with lidar data is the most important step in order to align photos and build historical orthomosaics with high horizontal accuracy. We produced two town-scale high-resolution historical orhomosaics from different timeframes (1934 and 1951) that vary in terms of spatial resolution—1934 (0.3 m/pixel) and 1951 (0.9 m/pixel). In terms of

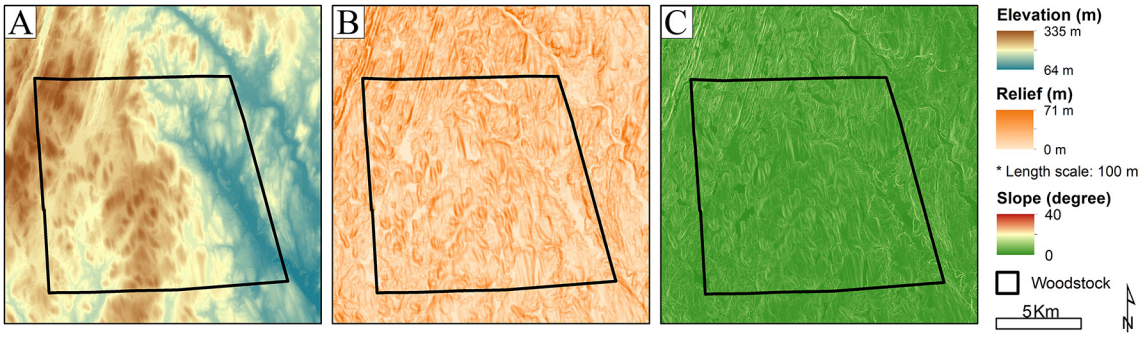

Figure 9. Map of three terrain elements (elevation, relief, and slope) in the study area.(A) elevation map; (B) relief map; (C) slope map.

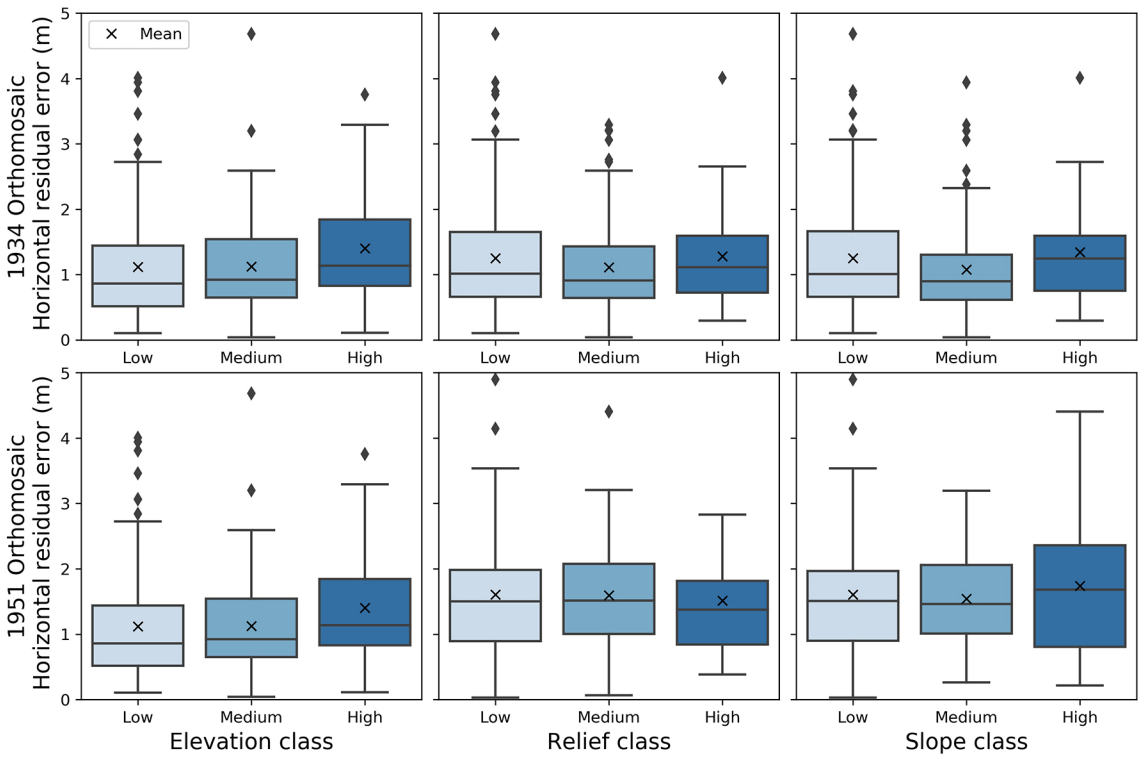

Figure 10. Residual error boxplots of three terrain elements (elevation, relief, and slope) reclassified into low, medium, and high classes based on a natural break. The top row shows the residual error results for the 1934 orthomosaic; the bottom row indicates that of the 1951 orthomosaic.

horizontal accuracy assessment, RMSE values without extreme outliers for both orthomosaics demonstrate they are highly accurate and can be used for standard mapping and GIS work according to 1990 ASPRS horizontal accuracy standard. In addition, the spatial distribution of CP residual errors indicates that an edge effect should be taken into account and enough photos should be included to cover at least one more edge layer larger than study area.

Moreover, we highlight that there are three factors influencing the quality of historical orthomosaics. First, it is important to use CPs not only extracted from high-resolution reference data such as lidar but also selected in terms of being stationary features through time and high frequency across the study area (e.g., stone walls and road crossings). Second, the number of tied photos can increase horizontal accuracy, but more tied photos do not always lead to higher accuracy because external causes such as image quality and stains on images prevent reference points being placed on the exact same locations. Lastly, it was found that the complexity of terrain can also affect the accuracy of orthomosaics.

Limitations to this study include the following: (1) the factors influencing the quality of historical orthomosaics were examined by a spatial join between the map of each factor and a map of CPs' residual errors such that it is not possible to examine the relationships amongst individual factors; (2) there may have been errors associated with orthomosaicking or accuracy assessments results due to digitization and imprecise locations of reference points on both photos and the map; and (3) it can be challenging to apply this method to completely forested areas where, in general, reference points are harder to come by.

Overall, despite these limitations, this contribution provides an important methodological procedure for making high-resolution, historical orthomosaics and for suggesting factors to be considered when applying this method. The procedure presented here can be applied to any study areas where historical aerial photographs and lidar data are available. Future application of this methodology would be to extend beyond the town scale considered here (e.g., 50–200 km²) all to the way to state scale or larger (10 000–100 000 km²), such as the state of Connecticut or the northeastern US in general. In addition to this, the outputs of our procedure can be used in various studies based on time-series analysis since the early to mid-20th century when historical aerial photographs become widely available, like detecting environmental disturbances, land use changes, and anthropogenic impacts. These products can also be used as input data for state-of-the-art deep learning algorithms to do image classification to reconstruct and analyze historical LULC.

Acknowledgments

This work was funded by a National Science Foundation grant BCS-1654462 to W. Ouimet. The authors wish to thank Katharine Johnson and Zhe Zhu for comments on an early draft of this contribution, and an anonymous reviewer for their helpful comments and suggestions.

References

Agisoft LLC. 2019. *Agisoft Metashape User Manual*. <https://www.agisoft.com/pdf/metashape-pro_1_5_en.pdf>.

Ajayi, O. G., A. A. Salubi, A. F. Angbas and M. G. Odigure. 2017. Generation of accurate digital elevation models from UAV acquired low percentage overlapping images. *International Journal of Remote Sensing* 38(8–10):3113–3134.

American Society for Photogrammetry and Remote Sensing. 1990. ASPRS accuracy standards for large-scale maps. *Photogrammetric Engineering & Remote Sensing* 56(7):1068–1070.

American Society for Photogrammetry and Remote Sensing. 2014. ASPRS positional accuracy standards for digital geospatial data, edition 1, version 1.0. *Photogrammetric Engineering & Remote Sensing* 81(3):1–26.

Arnaud, F., H. Piégay, L. Schmitt, A. J. Rollet, V. Ferrier and D. Béal. 2015. Historical geomorphic analysis (1932–2011) of a by-passed river reach in process-based restoration perspectives: the Old Rhine downstream of the Kembs Diversion Dam (France, Germany). *Geomorphology* 236:163–177.

Baker, W. L., J. J. Honaker and P. J. Weisberg. 1995. Using aerial photography and GIS to map the forest-tundra ecotone in Rocky Mountain National Park, Colorado, for global change research. *Photogrammetric Engineering and Remote Sensing* 61(3):313–320.

Bolstad, P. V. 1992. Geometric errors in natural resource GIS data: Tilt and terrain effects in aerial photographs. *Forest Science* 38(2):367–380.

Capitol Region Council of Governments (CRCoG). 2016. 2016 Aerial Imagery. <http://cteco.uconn.edu/data/flight2016/index.htm> Accessed on 29 July 2021.

Child, S. F., L. A. Stearns, L. Girod and H. H. Brecher. 2021. Structure-from-motion photogrammetry of antarctic historical aerial photographs in conjunction with ground control derived from satellite data. *Remote Sensing* 13(1):1–25.

Comiti, F., M. Da Canal, N. Surian, L. Mao, L. Picco and M. A. Lenzi. 2011. Channel adjustments and vegetation cover dynamics in a large gravel bed river over the last 200 years. *Geomorphology* 125(1):147–159.

Congalton, R. G. and K. Green. 2009. The photogrammetric record. In *Assessing the Accuracy of Remotely Sensed Data: Principles and Practices,* 2d ed. Boca Raton, Fla.: CRC Press.

Connecticut State Library. 1934. *1934 Aerial Surveys*. Record Group 089:011. College Park, Md.: Department of Transportation, State Archives.

Connecticut State Library. 1951. *1951 Aerial Surveys*. Record Group 089:011b. College Park, Md.: Department of Transportation, State Archives.

Cronon, W. 1983. *Changes in the Land: Indians, Colonists, and the Ecology of New England*. New York: Hill and Wang.

CT Environmental Conditions Online (CT ECO). 2012. 2012 Aerial Imagery. <http://cteco.uconn.edu/help/info_orthos2012.htm> Accessed on 29 July 2021.

ESRI. 2012. "World Topographic Map". 1:100 000. <http://www.arcgis.com/home/item.html?id=30e5fe3149c34df1ba922e6f5bbf808f> Accessed on 29 July 2021.

Fox, A. J. and A. Cziferszky. 2008. Unlocking the time capsule of historic aerial photography to measure changes in antarctic peninsula glaciers. *Photogrammetric Record* 23(121):51–68.

Frankl, A., V. Seghers, C. Stal, P. De Maeyer, G. Petrie and J. Nyssen. 2015. Using image-based modelling (SfM–MVS) to produce a 1935 orthomosaic of the Ethiopian highlands. *International Journal of Digital Earth* 8(5):421–430.

Gennaretti, F., M. N. Ripa, F. Gobattoni, L. Boccia and R. Pelorosso. 2011. A methodology proposal for land cover change analysis using historical aerial photos. *Journal of Geography and Regional Planning* 4(9):542–556.

Geyman, E. C., W. van Pelt, A. C. Maloof, H. F. Aas and J. Kohler. 2022. Historical glacier change on Svalbard predicts doubling of mass loss by 2100. *Nature* 601.

Gomez, C. 2014. Digital photogrammetry and GIS-based analysis of the bio-geomorphological evolution of Sakurajima Volcano, diachronic analysis from 1947 to 2006. *Journal of Volcanology and Geothermal Research* 280:1–13.

Hung, I.-K., D. Unger, D. Kulhavy and Y. Zhang. 2019. Positional precision analysis of orthomosaics derived from drone captured aerial imagery. *Drones* 3(2):46.

Johnson, K. M. and W. B. Ouimet. 2014. Rediscovering the lost archaeological landscape of southern New England using airborne light detection and ranging (LiDAR). *Journal of Archaeological Science* 43(1):9–20.

Johnson, K. M. and W. B. Ouimet. 2016. Physical properties and spatial controls of stone walls in the northeastern USA: Implications for anthropocene studies of 17th to early 20th century agriculture. *Anthropocene* 15:22–36.

Kadmon, R. and R. Harari-Kremer. 1999. Studying long-term vegetation dynamics using digital processing of historical aerial photographs. *Remote Sensing of Environment* 68:164–176.

Khan, Z. and S. J. Miklavcic. 2019. An automatic field plot extraction method from aerial orthomosaic images. *Frontiers in Plant Science* 10(May):1–13.

Leh, M., S. Bajwa and I. Chaubey. 2013. Impact of land use change on erosion risk: An integrated remote sensing, geographic information system and modeling methodology. *Land Degradation and Development* 421(2011):409–421.

Lingua, A., D. Marenchino and F. Nex. 2009. Performance analysis of the SIFT operator for automatic feature extraction and matching in photogrammetric applications. *Sensors* 9(5):3745–3766.

Llena, M., M. Cavalli, D. Vericat and S. Crema. 2018. Assessing landscape changes associated to anthropic disturbances by means of the application of structure from motion photogrammetry using historical aerial imagery. *Rendiconti Online Societa Geologica Italiana* 46(May):74–81.

Mallinis, G., D. Emmanoloudis, V. Giannakopoulos, F. Maris and N. Koutsias. 2011. Mapping and interpreting historical land cover/land use changes in a natura 2000 site using Earth observational data: The case of Nestos Delta, Greece. *Applied Geography* 31(1):312–320.

Marignani, M., D. Rocchini, D. Torri, A. Chiarucci and S. Maccherini. 2008. Planning restoration in a cultural landscape in Italy using an object-based approach and historical analysis. *Landscape and Urban Planning* 84(1):28–37.

Maurer, J. and S. Rupper. 2015. Tapping into the hexagon spy imagery database: A new automated pipeline for geomorphic change detection. *ISPRS Journal of Photogrammetry and Remote Sensing* 108:113–127.

Midgley, N. G. and T. N. Tonkin. 2017. Reconstruction of former glacier surface topography from archive oblique aerial images. *Geomorphology* 282:18–26.

National Research Council. 2001. Grand challenges in environmental sciences. In *Grand Challenges in Environmental Sciences*. Washington, DC: The National Academies Press.

Nebiker, S., N. Lack and M. Deuber. 2014. Building change detection from historical aerial photographs using dense image matching and object-based image analysis. *Remote Sensing* 6(9):8310–8336.

Nita, M. D., C. Munteanu, G. Gutman, I. V. Abrudan and V. C. Radeloff. 2018. Widespread forest cutting in the aftermath of World War II captured by broad-scale historical corona spy satellite photography. *Remote Sensing of Environment* 204:322–332.

Nogueira, F. C. and L. Roberto. 2017. Accuracy analysis of orthomosaic and DSM produced from sensor aboard UAV. In *XVIII Simpósio Brasileiro de Sensoriamento Remoto—SBSR*, 5515–5522.

Riquelme, A., M. Del Soldato, R. Tomás, M. Cano, L. Jordá Bordehore and S. Moretti. 2019. Digital landform reconstruction using old and recent open access digital aerial photos. *Geomorphology* 329:206–223.

Rocchini, D., G.L.W. Perry, M. Salerno, S. Maccherini and A. Chiarucci. 2006. Landscape change and the dynamics of open formations in a natural reserve. *Landscape and Urban Planning* 77(1–2):167–77.

Sevara, C. 2013. Top secret topographies: Recovering two and three-dimensional archaeological information from historic reconnaissance datasets using image-based modelling techniques. *International Journal of Heritage in the Digital Era* 2(3):395–418.

Thorson, R. M. 2002. *Stone by Stone : The Magnificent History in New England's Stone Walls*. New York, N.Y. : Walker & Company.

Tomaštík, J., M. Mokroš, P. Surový, A. Grznárová and J. Merganič. 2019. UAV RTK/PPK method—An optimal solution for mapping inaccessible forested areas? *Remote Sensing* 11(6):721.

Turner, D., A. Lucieer and C. Watson. 2012. An automated technique for generating georectified mosaics from ultra-high resolution unmanned aerial vehicle (UAV) imagery, based on structure from motion (SFM) point clouds. *Remote Sensing* 4(5):1392–1410.

Verbesselt, J., A. Zeileis and M. Herold. 2012. Near real-time disturbance detection using satellite image time series. *Remote Sensing of Environment* 123:98–108.

Verhoeven, G., M. Doneus, C. Briese and F. Vermeulen. 2012. Mapping by matching: A computer vision-based approach to fast and accurate georeferencing of archaeological aerial photographs. *Journal of Archaeological Science* 39(7):2060–2070.

Weng, J., T. S. Huang and N. Ahuja. 2013. *Motion and Structure from Image Sequences*. Berlin/Heidelberg, Germany: Springer Science & Business Media.

Wolf, P. R., B. A. Dewitt and B. E. Wilkinson. 2014. *Elements of Photogrammetry with Applications in GIS,* 4th ed. Columbus, Ohio: McGraw-Hill Education.

Zhu, Z. and C. E. Woodcock. 2014. Continuous change detection and classification of land cover using all available landsat data. *Remote Sensing of Environment* 144:152–171.

Zhu, Z., Y. Fu, C. E.Woodcock, P. Olofsson, J. E.Vogelmann, C. Holden, M. Wang, S. Dai and Y. Yu. 2016. Including land cover change in analysis of greenness trends using all available Landsat 5, 7, and 8 images: A case study from Guangzhou, China (2000–2014). *Remote Sensing of Environment* 185:243–257.

Zhu, Z., J. Zhang, Z. Yang, A. H. Aljaddani, W. B. Cohen, S. Qiu and C. Zhou. 2020. Continuous monitoring of land disturbance based on Landsat time series. *Remote Sensing of Environment* 238:111116.

Zomeni, M., J. Tzanopoulos and J. D. Pantis. 2008. Historical analysis of landscape change using remote sensing techniques: An explanatory tool for agricultural transformation in Greek rural areas. *Landscape and Urban Planning* 86(1):38–46.

IN-PRESS ARTICLES

Jordan Bowman, Lexie Yang, Orrin Thomas, Jerry Kirk, Andrew Duncan, David Hughes, and Shannon Meade. UAS Edge Computing of Energy Infrastructure Damage Assessment.

Firat Erdem, Nuri Erkin Ocer, Dilek Kucuk Matci, Gordana Kaplan, and Ugur Avdan. Apricot Tree Detection from UAV-Images Using Mask R-CNN and U-Net.

Batuhan Sariturk, Damla Kumbasar, and Dursun Zafer Seker. Comparative Analysis of Different CNN Models for Building Segmentation from Satellite and UAV Images.

Rabi N. Sahoo, Shalini Gakhar, R.G. Rejith, Rajeev Ranjan, Mahesh C. Meena, Abir Dey, Joydeep Mukherjee, Rajkumar Dhakar, Sunny Arya, Anchal Daas, Subhash Babu, Pravin K. Upadhyay, Kapila Sekhawat, Sudhir Kumar, Mahesh Kumar, Viswanathan Chinnusamy, and Manoj Khanna. Unmanned Aerial Vehicle (UAV)–Based Imaging Spectroscopy for Predicting Wheat Leaf Nitrogen.

Yunus Kaya, Halil İbrahim Şenol, Abdurahman Yasin Yiğit, and Murat Yakar. Car Detection from Very High-Resolution UAV Images Using Deep Learning Algorithms.

Xin Jia, Qing Zhu, Xuming Ge, Ruifeng Ma, Daiwei Zhang, and Tao Liu. Robust Guardrail Instantiation and Trajectory Optimization of Complex Highways Based on Mobile Laser Scanning Point Clouds.

Shuanggen Jin, Ayman M.Elameen, Daniel Olago. Identification of drought events in major basins of Africa based on weighted water storage deficit index from GRACE measurements.

Xin Jia, Qing Zhu, Xuming Ge, Ruifeng Ma, Daiwei Zhang, and Tao Liu. Robust Guardrail Instantiation and Trajectory Optimization of Complex Highways Based on Mobile Laser Scanning Point Clouds.

Zhikang Lin, Wei Liu, Yulong Wang, Yan Xu, Chaoyang Niu. Change Detection in SAR Images through Clustering Fusion Algorithm and Deep Neural Networks.

Dan Li, Hanjie Wu, Yujian Wang, Xiaojun Li, Fanqiang Kong, and Qiang Wang. Lightweight Parallel Octave Convolutional Neural Network for Hyperspectral Image Classification.

Tolga Bakirman, Bahadir Kulavuz, and Bulent Bayram. Use of Artificial Intelligence Toward Climate-Neutral Cultural Heritage.

The Cellular Automata Approach in Dynamic Modelling of Land Use Change Detection and Future Simulations Based on Remote Sensing Data in Lahore Pakistan

Muhammad Nasar Ahmad, Zhenfeng Shao, Akib Javed, Fakhrul Islam, Hafiz Haroon Ahmad, and Rana Waqar Aslam

Abstract

Rapid urbanization has become an immense problem in Lahore city, causing various socio-economic and environmental problems. Therefore, it is noteworthy to monitor land use/land cover (LULC) change detection and future LULC patterns in Lahore. The present study focuses on evaluating the current extent and modeling the future LULC developments in Lahore, Pakistan. Therefore, the semi-automatic classification model has been applied for the classification of Landsat satellite imagery from 2000 to 2020. And the Modules of Land Use Change Evaluation (MOLUSCE) cellular automata (CA-ANN) model was implemented to simulate future land use trends for the years 2030 and 2040. This study project made use of Landsat, Shuttle Radar Topography Mission Digital Elevation Model, and vector data. The research methodology includes three main steps: (i) semi-automatic land use classification using Landsat data from 2000 to 2020; (ii) future land use prediction using the CA-ANN (MOLUSCE) model; and (iii) monitoring change detection and interpretation of results. The research findings indicated that there was a rise in urban areas and a decline in vegetation, barren land, and water bodies for both the past and future projections. The results also revealed that about 27.41% of the urban area has been increased from 2000 to 2020 with a decrease of 42.13% in vegetation, 2.3% in barren land, and 6.51% in water bodies, respectively. The urban area is also expected to grow by 23.15% between 2020 and 2040, whereas vegetation, barren land, and water bodies will all decline by 28.05%, 1.8%, and 12.31%, respectively. Results can also aid in the long-term, sustainable planning of the city. It was also observed that the majority of the city's urban area expansion was found to have occurred in the city's eastern and southern regions. This research also suggests that decision-makers and municipal Government should reconsider city expansion strategies. Moreover, the future city master plans of 2050 must emphasize the relevance of rooftop urban planting and natural resource conservation.

Introduction

Land use describes how people use the land, while land cover refers to the characteristics of the surface materials. Rapid transformation in land use/land cover (LULC) affects the human environment (Guidigan *et al.* 2019; Hou *et al.* 2020) and ecosystem services (Chen *et al.* 2021; Huang *et al.* 2019). Over the past two decades, LULC change detection has drawn a lot of attention from researchers. Land use/land cover is primarily expedited by the construction of artificial infrastructure (Girma *et al.* 2022; Zhu *et al.* 2022). Therefore, significant change in LULC has been influenced by rapid urbanization (Li *et al.* 2019; Naikoo *et al.* 2022) and population growth all over the world. As a result of rapid urbanization and infrastructure development, mostly vegetation and water bodies have changed into urban centers (Dewan and Yamaguchi 2009; Hassan 2017). By 2050, it is projected that the metropolitan sectors will increase by 66% (Marondedze and Schütt 2021; Ullah *et al.* 2019).

There are several key issues driven by LULC change which are: increase in land surface temperature, haze, smog, vegetation loss, increase in impervious surface (Nath *et al.* 2021), environmental uncertainties, CO_2 emissions (Bhattacharjee and Chen 2020; Zhou *et al.* 2021), water degradation, and urban flooding. In the cities, a high proportion of vegetation cover is converted into impervious surfaces due to recent metropolitan expansions. Therefore, for a better knowledge of prior research on LULC, it is important to monitor existing trends and the future trajectory of LULC detection.

Remote sensing (Sohl and Sleeter 2012) combined with geo-information science has provided a new corridor for researchers to conduct studies related to urban development. Advancements in remote sensing technologies such as machine learning and artificial intelligence technologies (Abbas *et al.* 2021; Hamedianfar *et al.* 2020; Talukdar *et al.* 2020) are providing prompt and reliable results. There are numerous prediction models adopted by researchers (Ghalehteimouri *et al.* 2022; Zhang *et al.* 2022), such as Markov Chain, Artificial Neural Network (ANN), and cellular automata (CA). The cellular automata model is used more extensively to simulate future LULC change as it uses historical LULC data (Akbar *et al.* 2019; Guidigan *et al.* 2019) with independent variables to strengthen the prediction results. Cellular automata is a well-known and well-adopted artificial intelligence modeling technique (Al-Darwish *et al.* 2018). The CA model operates in such a manner that it computes cells automatically based on transitional rules and algorithm equations, and it simulates complex systems such as city expansion dynamics (Khan *et al.* 2022; Shafizadeh-Moghadam *et al.* 2021; Zhang and Wang 2021).

This research work was conducted based on CA and ANN algorithms using the Modules for Land-use Change Evaluation (MOLUSCE) model. Moreover, the machine learning-based model of semi-automatic classification (SCP) is used for land-use classification. MOLUSCE uses Markov chain analysis and cellular automata methods (Aneesha Satya *et al.* 2020) to determine the land-use dynamics.

Muhammad Nasar Ahmad, Zhenfeng Shao, Akib Javed, and Rana Waqar Aslam are with the State Key Laboratory of Information Engineering in Surveying, Mapping and Remote Sensing, Wuhan University, Wuhan 430079, China (mnasarahmad@whu.edu.cn).

Fakhrul Islam is with Khushal Khan Khattak University, Karak, Khyber Pakhtunkhwa, Pakistan.

Hafiz Haroon Ahmad is with the School of Space and Earth Sciences, University of Science and Technology of China, Hefei, Anhui, 230026, China.

Contributed by Prasad S. Thenkabail, July 19, 2022 (sent for review August 21, 2022; reviewed by Agnes Begue, Bingqing Liang).

Photogrammetric Engineering & Remote Sensing
Vol. 89, No. 1, January 2023, pp. 47–55.
0099-1112/22/47–55

doi: 10.14358/PERS.22-00102R2

Call for *PE&RS* Special Issue Submissions

Innovative Methods for Geospatial Data using Remote Sensing and GIS

Internationally comparable data is a global need for managing resources, monitoring current trends and taking actions for sustainable living. Even though there has been a significant progress on geospatial data availability, extensive data gaps are still a major problem for general assessment and supervise the progress through the years. According to United Nations 2022 The Sustainable Development Goals Report, while health and energy sectors have the highest data available, limited data available for climate action.

The COVID-19 crisis has also shown that there are innovative data collection methods utilizing information and computer technologies. However, only 5% of the countries have benefit from remote sensing technologies to measure the impact of COVID-19. Additionally, novel approaches such as artificial intelligence should be used in conjunction with assessments to make sure they are put to use for critical situations.

The recent developments in remote sensing, geographic information systems and ICT have provided a wide accessibility to create geospatial data for various purposes. The proposed special issue focuses on *"Innovative Methods for Geospatial Data using Remote Sensing and GIS" for wide range of applications. This special issue aims to bring researchers to share knowledge and their expertise about innovative methods to contribute to fill data gaps around the world for a better future.*

The proposed special issue aims to contributes ASPRS's key mission on 'Simplify and promote the use of image-based geospatial technologies for the end-user', 'Promote collaboration between end users and geospatial experts to match data and technology to applications and solutions' and 'promote the transfer of geospatial data and information technology to developing nations' by providing innovative methods to create geospatial data using remote sensing and geographic information systems utilizing state-of-the-art developments and solutions.

Deadline for Manuscript Submission—July 1, 2023

Submit your Manuscript to http://asprs-pers.edmgr.com

Guest Editors

Dr. Tolga Bakirman, bakirman@yildiz.edu.tr , *Yildiz Technical University, Department of Geomatic Engineering*, Davutpasa Campus, 34220 Esenler-Istanbul/Turkey

Dr. George Arampatzis, garampatzis@pem.tuc.gr, *Technical University Crete, School of Production Engineering & Management*, 73100 Chania – Crete/Greece

WHO'S WHO IN ASPRS

Founded in 1934, the American Society for Photogrammetry and Remote Sensing (ASPRS) is a scientific association serving thousands of professional members around the world. Our mission is to advance knowledge and improve understanding of mapping sciences to promote the responsible applications of photogrammetry, remote sensing, geographic information systems (GIS) and supporting technologies.

BOARD OF DIRECTORS

BOARD OFFICERS

President
Christopher Parrish, Ph.D
Oregon State University

President-Elect
Lorraine B. Amenda, PLS, CP
Towill, Inc.

Vice President
Bandana Kar
Oak Ridge National Lab

Past President
Jason M. Stoker, Ph.D,
U.S. Geological Survey

Treasurer
John McCombs
NOAA

Secretary
Harold Rempel
ESP Associates, Inc.

COUNCIL OFFICERS

ASPRS has six councils. To learn more, visit https://www.asprs.org/Councils.html.

Sustaining Members Council
Chair: Ryan Bowe
Deputy Chair: Melissa Martin

Technical Division Directors Council
Chair: Bill Swope
Deputy Chair: Hope Morgan

Standing Committee Chairs Council
Chair: David Stolarz
Deputy Chair: TBA

Early-Career Professionals Council
Chair: Madeline Stewart
Deputy Chair: Kyle Knapp

Region Officers Council
Chair: Demetrio Zourarakis
Deputy Chair: Jason Krueger

Student Advisory Council
Chair: Lauren McKinney-Wise
Deputy Chair: Oscar Duran

TECHNICAL DIVISION OFFICERS

ASPRS has seven professional divisions. To learn more, visit https://www.asprs.org/Divisions.html.

Geographic Information Systems Division
Director: Denise Theunissen
Assistant Director: Jin Lee

Lidar Division
Director: Ajit Sampath
Assistant Director: Mat Bethel

Photogrammetric Applications Division
Director: Ben Wilkinson
Assistant Director: Hank Theiss

Primary Data Acquisition Division
Director: Greg Stensaas
Assistant Director: Srini Dharmapuri

Professional Practice Division
Director: Bill Swope
Assistant Director: Hope Morgan

Remote Sensing Applications Division
Director: Amr Abd-Ehrahman
Assistant Director: Tao Liu

Unmanned Autonomous Systems (UAS)
Director: Jacob Lopez
Assistant Director: Bahram Salehi

REGION PRESIDENTS

ASPRS has 13 regions to serve the United States. To learn more, visit https://www.asprs.org/regions.html.

Alaska Region

Cascadia Region
Robert Hariston-Porter

Eastern Great Lakes Region
Michael Joos, CP, GISP

Florida Region
Xan Fredericks

Heartland Region
Whit Lynn

Intermountain Region
Robert T. Pack

Mid-South Region
David Hughes

Northeast Region

North Atlantic Region

Pacific Southwest Region
John Erickson, PLS, CP

Potomac Region
Dave Lasko

Rocky Mountain Region

Western Great Lakes Region
Adam Smith

SUSTAININGMEMBERS

ACI USA Inc.
Weston, Florida
https://acicorporation.com/
Member Since: 2/2018

Aerial Services, Inc.
Cedar Falls, Iowa
www.AerialServicesInc.com
Member Since: 5/2001

Airworks Solutions Inc.
Boston, Massachusetts
Member Since: 3/2022

Applanix
Richmond Hill, Ontario, Canada
http://www.applanix.com
Member Since: 7/1997

Ayres Associates
Madison, Wisconsin
www.AyresAssociates.com
Member Since: 1/1953

CT Consultants
Mentor, Ohio
Member Since: 3/2022

Dewberry
Fairfax, Virginia
www.dewberry.com
Member Since: 1/1985

Esri
Redlands, California
www.esri.com
Member Since: 1/1987

GeoCue Group
Madison, Alabama
http://www.geocue.com
Member Since: 10/2003

Geographic Imperatives LLC
Centennial, Colorado
Member Since: 12/2020

GeoWing Mapping, Inc.
Richmond, California
www.geowingmapping.com
Member Since: 12/2016

Halff Associates, Inc.
Richardson, Texas
www.halff.com
Member Since: 8/2021

Keystone Aerial Surveys, Inc.
Philadelphia, Pennsylvania
www.kasurveys.com
Member Since: 1/1985

Kucera International
Willoughby, Ohio
www.kucerainternational.com
Member Since: 1/1992

L3Harris Technologies
Broomfield, Colorado
www.l3harris.com
Member Since: 6/2008

Merrick & Company
Greenwood Village, Colorado
www.merrick.com/gis
Member Since: 4/1995

Nearmap
South Jordan, Utah
www.nearmap.com
Member Since: 6/2023

NV5 Geospatial
Sheboygan Falls, Wisconsin
www.quantumspatial.com
Member Since: 1/1974

Pickett and Associates, Inc.
Bartow, Florida
www.pickettusa.com
Member Since: 4/2007

Riegl USA, Inc.
Orlando, Florida
www.rieglusa.com
Member Since: 11/2004

Robinson Aerial Surveys, Inc.(RAS)
Hackettstown, New Jersey
www.robinsonaerial.com
Member Since: 1/1954

Sanborn Map Company
Colorado Springs, Colorado
www.sanborn.com
Member Since: 10/1984

Surdex Corporation
Chesterfield, Missouri
www.surdex.com
Member Since: 12/2011

Surveying And Mapping, LLC (SAM)
Austin, Texas
www.sam.biz
Member Since: 12/2005

T3 Global Strategies, Inc.
Bridgeville, Pennsylvania
https://t3gs.com/
Member Since: 6/2020

Towill, Inc.
San Francisco, California
www.towill.com
Member Since: 1/1952

Woolpert LLP
Dayton, Ohio
www.woolpert.com
Member Since: 1/1985

SUSTAININGMEMBER**BENEFITS**

Membership

- ✓ Provides a means for dissemination of new information
- ✓ Encourages an exchange of ideas and communication
- ✓ Offers prime exposure for companies

Benefits of an ASPRS Membership

- Complimentary and discounted Employee Membership*
- E-mail blast to full ASPRS membership*
- Professional Certification Application fee discount for any employee
- Member price for ASPRS publications
- Discount on group registration to ASPRS virtual conferences
- Sustaining Member company listing in ASPRS directory/website
- Hot link to company website from Sustaining Member company listing page on ASPRS website
- Press Release Priority Listing in *PE&RS* Industry News
- Priority publishing of Highlight Articles in *PE&RS* plus, 20% discount off cover fee
- Discount on *PE&RS* advertising
- Exhibit discounts at ASPRS sponsored conferences (exception ASPRS/ILMF)
- Free training webinar registrations per year*
- Discount on additional training webinar registrations for employees
- Discount for each new SMC member brought on board (Discount for first year only)

*quantity depends on membership level

PE&RS 2023 Advertising Rates & Specs

THE MORE YOU ADVERTISE THE MORE YOU SAVE! *PE&RS* offers frequency discounts. Invest in a three-times per year advertising package and receive a 5% discount, six-times per year and receive a 10% discount, 12-times per year and receive a 15% discount off the cost of the package.

	Sustaining Member Exhibiting at a 2023 ASPRS Conference	**Sustaining Member**	**Exhibitor**	**Non Member**
All rates below are for four-color advertisments				
Cover 1	$1,850	$2,000	$2,350	$2,500
In addition to the cover image, the cover sponsor receives a half-page area to include a description of the cover (maximum 500 words). The cover sponsor also has the opportunity to write a highlight article for the journal. Highlight articles are scientific articles designed to appeal to a broad audience and are subject to editorial review before publishing. The cover sponsor fee includes 50 copies of the journal for distribution to their clients. More copies can be ordered at cost.				
Cover 2	$1,500	$1,850	$2,000	$2,350
Cover 3	$1,500	$1,850	$2,000	$2,350
Cover 4	$1,850	$2,000	$2,350	$2,500
Advertorial	1 Complimentary Per Year	1 Complimentary Per Year	$2,150	$2,500
Full Page	$1,000	$1,175	$2,000	$2,350
2 page spread	$1,500	$1,800	$3,200	$3,600
2/3 Page	$1,100	$1,160	$1,450	$1,450
1/2 Page	$900	$960	$1,200	$1,200
1/3 Page	$800	$800	$1,000	$1,000
1/4 Page	$600	$600	$750	$750
1/6 Page	$400	$400	$500	$500
1/8 Page	$200	$200	$250	$250
Other Advertising Opportunities				
Employment Promotion	$500 (30 day web + 1 email) $300 (30 day web)	$500 (30 day web + 1 email) $300 (30 day web)	$500 (30 day web + 1 email) $300 (30 day web)	$500 (30 day web + 1 email) $300 (30 day web)
Dedicated Content Email blast	$3000	$3000	$3000	$3000
Newsletter Display Advertising	1 Complimentary Per Year	1 Complimentary Per Year	$500	$500
PE&RS Digital Edition Announcement E-Mail	$1000	$1000	$1000	$1000

A 15% commission is allowed to recognized advertising agencies

Ad Size	**Width**	**Height**
Cover (bleed only)	8.625"	11.25"
Full Page (bleed)	8.625"	11.25"
Full Page (trim)	8.375"	10.875"
2/3 Page Horizontal	7.125"	6.25"
2/3 Page Vertical	4.58"	9.625"
1/2 Page Horizontal	7.125"	4.6875"
1/2 Page Vertical	3.4375"	9.625"
1/3 Page Horizontal	7.125"	3.125"
1/3 Page Vertical	2.29"	9.625"
1/4 Page Horizontal	7.125"	2.34"
1/4 Page Vertical	3.4375"	4.6875"
1/8 Page Horizontal	7.125"	1.17"
1/8 Page Vertical	1.71875"	4.6875"

- Publication Size: 8.375" × 10.875" (W x H)
- Live area: 1/2" from gutter and 3/8" from all other edges
- No partial page bleeds
- Publication Style: Perfect bound
- Printing Method: Web offset press
- Software Used: PC InDesign
- Supported formats:
  TIFF, EPS, BMP, JPEG, PDF, PNG
  PC InDesign, Illustrator,
  and Photoshop

Send ad materials to:
Rae Kelley
rkelley@asprs.org

Ship inserts to:
Alicia Coard
Walsworth
2180 Maiden Lane
St. Joseph, MI 49085
888-563-3220 (toll free)
269-428-1021 (direct)
269-428-1095 (fax)
alicia.coard@walsworth.com

Special Advertising Opportunities

FRONT COVER SPONSORSHIP

A *PE&RS* cover sponsorship is a unique opportunity to capture the undivided attention of your target market through three premium points of contact.

1— *PE&RS* FRONT COVER

(Only twelve available, first-come, first-served)
PE&RS is world-renowned for the outstanding imagery displayed monthly on its front cover—and readers have told us they eagerly anticipate every issue. This is a premium opportunity for any company, government agency, university or non-profit organization to provide a strong image that demonstrates their expertise in the geospatial information industry.

2— FREE ACCOMPANYING "HIGHLIGHT" ARTICLE

A detailed article to enhance your cover image is welcome but not a condition of placing an image. Many readers have asked for more information about the covers and your article is a highly visible way to tell your story in more depth for an audience keenly interested in your products and services. No article is guaranteed publication, as it must pass ASPRS editorial review. For more information, contact Rae Kelley at rkelley@asprs.org.

3— FREE TABLE OF CONTENTS COVER DESCRIPTION

Use this highly visible position to showcase your organization by featuring highlights of the technology used in capturing the front cover imagery. Limit 200-word description.

Terms: Fifty percent nonrefundable deposit with space reservation and payment of balance on or before materials closing deadline.

Cover Specifications: Bleed size: 8 5/8" × 11 1/4", Trim: 8 3/8" × 10 7/8"

PRICING

	Sustaining Member Exhibiting at a 2023 ASPRS Conference	Sustaining Member	Exhibitor	Non Member
Cover 1	$1,850	$2,000	$2,350	$2,500

Belly Bands, Inserts, Outserts & More!

Make your material the first impression readers have when they get their copy of *PE&RS*. Contact Bill Spilman at bill@innovativemediasolutions.com

VENDOR SEMINARS

ASPRS Sustaining Members now have the opportunity to hold a 1-hour informational session as a Virtual Vendor Seminar that will be free to all ASPRS Members wishing to attend. There will be one opportunity per month to reach out to all ASPRS Members with a demonstration of a new product, service, or other information. ASPRS will promote the Seminar through a blast email to all members, a notice on the ASPRS web site home page, and ads in the print and digital editions of *PE&RS*.

The Virtual Seminar will be hosted by ASPRS through its Zoom capability and has the capacity to accommodate 500 attendees.

Vendor Seminars	
Fee	$2,500 (no discounts)

DIGITAL ADVERTISING OPPORTUNITIES

EMPLOYMENT PROMOTION

When you need to fill a position right away, use this direct, right-to-the-desktop approach to announce your employment opportunity. The employment opportunity will be sent once to all ASPRS members in our regular Wednesday email newsletter to members, and will be posted on the ASPRS Web site for one month. This type of advertising gets results when you provide a web link with your text.

Employment Opportunity	Net Rate
30-Day Web + 1 email	$500/opportunity
Web-only (no email)	$300/opportunity

Do you have multiple vacancies that need to be filled? Contact us for pricing details for multiple listings.

NEWSLETTER DISPLAY ADVERTISING

Your vertical ad will show up in the right hand column of our weekly newsletter, which is sent to more than 3,000 people, including our membership and interested parties. **Open Rate: 32.9%**

Newsletter vertical banner ad	Net Rate
180 pixels x 240 pixels max	$500/opportunity

DEDICATED CONTENT EMAIL BLAST

Send a dedicated email blast to the ASPRS email list. Advertiser supplies HTML (including images). Lead time: 14 days.

Materials	Net Rate
Advertiser supplies HTML, including images.	$3000/ opportunity

PE&RS Digital Edition

Digital Edition Announcement E-Mail: 5,800+

PE&RS is available online in both a public version that is available to anyone but does not include the peer-reviewed articles, and a full version that is available to ASPRS members only upon login.

The enhanced version of *PE&RS* contains hot links for all ASPRS Sustaining Member Companies, as well as hot links on advertisements, ASPRS Who's Who, and internet references.

Become a sponsor today!

The e-mail blast sponsorship opportunity includes a **180 x 240 pixel ad** in the email announcement that goes out to our membership announcing the availability of the electronic issue.

Digital Edition Opportunities	Net Rate
E-mail Blast Sponsorship*	$1,000

Landsat's Enduring Legacy

Pioneering Global Land Observations from Space

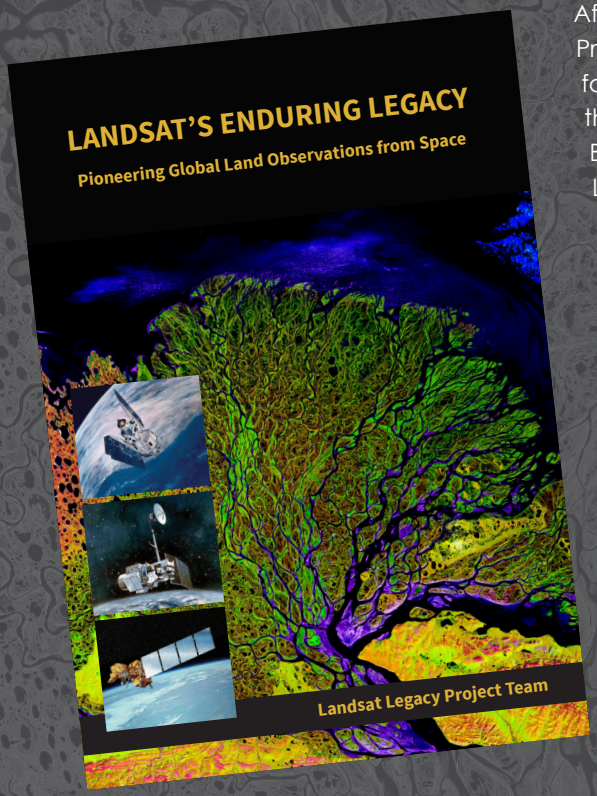

After more than 15 years of research and writing, the Landsat Legacy Project Team published, in collaboration with the American Society for Photogrammetry and Remote Sensing (ASPRS), a seminal work on the nearly half-century of monitoring the Earth's lands with Landsat. Born of technologies that evolved from the Second World War, Landsat not only pioneered global land monitoring but in the process drove innovation in digital imaging technologies and encouraged development of global imagery archives. Access to this imagery led to early breakthroughs in natural resources assessments, particularly for agriculture, forestry, and geology. The technical Landsat remote sensing revolution was not simple or straightforward. Early conflicts between civilian and defense satellite remote sensing users gave way to disagreements over whether the Landsat system should be a public service or a private enterprise. The failed attempts to privatize Landsat nearly led to its demise. Only the combined engagement of civilian and defense organizations ultimately saved this pioneer satellite land monitoring program. With the emergence of 21st century Earth system science research, the full value of the Landsat concept and its continuous 45-year global archive has been recognized and embraced. Discussion of Landsat's future continues but its heritage will not be forgotten.

The pioneering satellite system's vital history is captured in this notable volume on Landsat's Enduring Legacy.

Landsat Legacy Project Team

Samuel N. Goward
Darrel L. Williams
Terry Arvidson
Laura E. P. Rocchio
James R. Irons
Carol A. Russell
Shaida S. Johnston

Landsat's Enduring Legacy

Hardback. 2017, ISBN 1-57083-101-7

Member/Non-member	$48*
Student Member	$36*

* Plus shipping

Order online at

www.asprs.org/landsat

asprs THE IMAGING & GEOSPATIAL INFORMATION SOCIETY